Nonlinear Mirror Mode Dynamics: Simulations and Modeling

F. Califano,[1] P. Hellinger,[2] E. Kuznetsov,[3] T. Passot,[4] P.L. Sulem[4] and P. Trávníček[2]

Abstract. With the aim to understand the origin of the pressure-balanced magnetic structures in the form of holes and humps commonly observed in the solar wind and planetary magnetosheaths, high-resolution hybrid numerical simulations of the Vlasov-Maxwell (VM) equations using both Lagrangian (particle in cells) and Eulerian integration schemes are presented and compared with asymptotic and phenomenological models for the nonlinear mirror mode dynamics. It turns out that magnetic holes do not result from direct nonlinear saturation of the mirror instability that rather leads to magnetic humps. Nevertheless, both above and below threshold, there exist stable solutions of the VM equations in the form of large-amplitude magnetic holes. Special attention is paid to the skewness of the magnetic fluctuations (that is negative for holes and positive for humps) and its dependency on the distance to threshold and the beta of the plasma. Furthermore, the long-time evolution of magnetic humps resulting from the mirror instability in an extended domain far enough from threshold may, when the beta of the plasma is not too large, eventually lead to the formation of magnetic holes.

1. Introduction

Since the first observations of *Kaufmann et al.* [1970], a strong interest has been paid to the pressure-balanced magnetic structures observed in regions of the solar wind and of planetary magnetosheaths where β is relatively large and the ion perpendicular temperature exceeds the parallel one. These structures that are static in the plasma frame, display a strong anticorrelation between magnetic intensity and pressure as well as density variations. Their shape is cigar-like, elongated along a direction making a small angle with the ambient magnetic field [*Horbury et al.*, 2004, and references therein]. Early observations tended to suggest a predominance of magnetic holes [*Sperveslage et al.*, 2000], but more recent data indicate that magnetic humps are also frequently encountered [*Lucek et al.*, 1999; *Joy et al.*, 2006; *Soucek et al.*, 2008]. Recently, *Joy et al.* [2006] correlate the existence of magnetic holes or humps with the relatively small or large value of β. *Génot et al.* [2006] used a more quantitative characterization of the statistically dominant type of magnetic structures by measuring the degree of skewness that reflects the preference towards magnetic holes or humps, depending of its negative or positive sign. Similar analyses were performed by *Soucek et al.* [2008] after wavelet filtering of the data. It turns out that there exists a clear statistical correlation between the skewness and the distance to the mirror instability threshold. Slightly above threshold, quasi-sinusoidal fluctuations dominate, while at further distance (which often corresponds to larger values of β), magnetic humps are preferably observed. Magnetic holes are mainly observed both below threshold and slightly above in a range corresponding to ion (proton) $\beta_\parallel \leq 5$ and a temperature anisotropy empirically fitted as $T_\perp/T_\parallel \leq 2.15/\beta_\parallel^{0.39}$ [*Soucek et al.*, 2008].

The nature and the origin of these structures remains the object of different interpretations. *Stasiewicz* [2004a] interprets them as magnetosonic solitons, an approach initiated by *Baumgärtel et al.* [1997] (see also [*Baumgärtel*, 1999]). A more general opinion nevertheless associates them to nonlinearly saturated mirror modes. Such an origin, although plausible, is however not fully established. In realistic situations, the mirror instability is often competing with the anisotropic ion cyclotron instability, especially at β of order unity and moderate angles [*Price et al.*, 1986; *McKean et al.*, 1992], although the presence of helium He^{++} can enhance the relative importance of the former effect [*Price et al.*, 1986; *McKean et al.*, 1994].

The question arises of the driver of these instabilities, probably associated with the shock transition and the compression/expansion of the magnetosheath plasma [*Hellinger and Trávníček*, 2005; *Trávníček et al.*, 2007], which may increase the ratio between the perpendicular and parallel temperatures. The detailed mechanism of such processes, albeit of great importance, are nevertheless difficult to include in numerical simulations of the mirror instability. As a consequence, most of numerical simulations assume a bi-Maxwellian distribution and a collisionless plasma, conditions that are consistent with the separation between the time scale of the addressed phenomena and that of collisional effects. In this context, previous numerical integrations of VM equations, using hybrid particle-in-cell (PIC) methods [*Baumgärtel et al.*, 2003] have shown saturation of the mirror instability in the form of magnetic humps and not holes. These authors nevertheless also noted that initial conditions in the form of large-amplitude magnetic holes can persist during the whole simulation, both when the plasma is linearly stable and unstable, indicating the existence of a bistable regime.

It is thus of interest to study in detail the nonlinear development of the mirror instability. The linear regime has been extensively investigated and it is now well known that Landau and finite Larmor radius (FLR) effects play an essential role in the instability growth rate [*Vedenov and Sagdeev*, 1959; *Hasegawa*, 1969; *Hall*, 1979; *Gary*, 1992; *Southwood and Kivelson*, 1993; *Pokhotelov et al.*, 2005; *Hellinger*, 2007]. In contrast, the understanding of the nonlinear regime and of the origin of the saturating processes is more limited. The quasi-linear theory that assumes random-phase fluctuations was first suggested by *Shapiro and Shevchenko* [1964]. Nevertheless, this approach cannot apply to regimes dominated by coherent structures. Phenomenological models, based on the cooling of trapped particles in magnetic troughs [*Kivelson and Southwood*, 1996; *Pantellini*, 1998], were then developed to interpret the existence of deep magnetic holes. These models are however hardly consistent with the presence of magnetic humps that are only predicted for exceptionally large values of β. The possible existence of bistability is also not reproduced. Furthermore, these models are aimed to describe the microscopic processes associated with the existence of static coherent structures, rather than the dynamical processes leading to their formation.

[1]Dipartimento di Fisica and CNISM, Università di Pisa, Italy
[2]Institute of Atmospheric Physics, AS CR, Prague, Czech Republic
[3]Lebedev Physical Institute and Landau Institute of Theoretical Physics, Moscow, Russia
[4]Université de Nice-Sophia Antipolis, CNRS, Observatoire de la Côte d'Azur, Nice, France

0148-0227/08/2007JA012898$9.00

In order to study the formation of coherent structures as the nonlinear development of the mirror instability, an asymptotic analysis near threshold, based on a reductive perturbative expansion of VM equations was recently proposed. In this limit, the linearly unstable modes are confined at large scales, which suggests that FLR corrections arise at a linear level only, making the nonlinear contributions amenable to a simplified computation in the framework of the drift-kinetic equation [*Kuznetsov et al.*, 2007a]. The resulting asymptotic equation indicates that the retained nonlinearities reinforce the mirror instability, leading to a finite-time singularity associated with a subcritical bifurcation [*Kuznetsov et al.*, 2007b] and an early breaking of the asymptotic scalings. Nonlinear kinetic effects then rapidly become relevant and saturate the instability in a regime not amenable to a perturbative approach.

The aim of the present paper is to contribute to a better understanding of the nonlinear dynamics of mirror modes in a proton-electron homogeneous plasma, by means of highly accurate numerical simulations and asymptotic models. Vlasov-Maxwell equations are used for the proton distribution function, while a fluid description is assumed for the electrons that are assumed to be cold and massless for an easier comparison with theoretical developments. Section 2 is a short overview of the linear and quasi-linear theories. Section 3 briefly describes the algorithms implemented in the hybrid PIC and Eulerian simulations presented in the following sections. Section 4 discusses the results of numerical simulations near threshold, and points out the influence of the size of the domain on the early nonlinear phase. Special attention is paid to the conditions for the emergence of a quasi-linear phase that precedes the structure formation. Section 5 describes a reductive perturbative expansion directly performed on the VM equations, that provides a systematic derivation of the asymptotic equation derived in *Kuznetsov et al.* [2007a]. As already mentioned, this equation displays a finite time singularity, associated with a subcritical bifurcation, leading, near threshold, to the formation of large-amplitude structures, not amenable to a perturbative calculation. Supplementing phenomenologically the effects of the local variation of the ion Larmor radius nevertheless provides a simple model for the nonlinear saturation, in good agreement with numerical simulations and spatial observations [*Génot et al.*, 2006; *Soucek et al.*, 2008], while models involving a saturation resulting from particle trapping [*Kivelson and Southwood*, 1996; *Pantellini*, 1998; *Pokhotelov et al.*, 2007] are unable to reproduce the geometry of the created mirror structures. Section 6 provides numerical evidence of the persistence of initially assumed large-amplitude magnetic depressions both in the mirror stable and unstable plasmas. In section 7 we present a simulation which demonstrates that in an extended domain far from threshold magnetic humps generated by the mirror instability can transform to magnetic holes during the long-time evolution. Section 8 summarizes the results and discusses a few open problems.

2. Brief overview of the linear and quasi-linear theories

Before presenting numerical simulations of the mirror instability in an electron-proton plasma, it is useful to briefly review the linear and quasi-linear theories.

For a gyrotropic proton distribution function $f^{(0)} = f^{(0)}(v_\parallel^2, v_\perp)$ and cold electrons, the mirror instability condition is given by [*Shapiro and Shevchenko*, 1964; *Pokhotelov et al.*, 2005; *Hellinger*, 2007]

$$\Gamma \equiv -\frac{m_p}{p_B}\int \frac{v_\perp^4}{4}\frac{\partial f^{(0)}}{\partial v_\parallel^2}d^3v - \beta_\perp - 1 > 0 \qquad (1)$$

where $p_B = B_0^2/8\pi$ is the magnetic pressure, $\beta_\perp = m_p\int v_\perp^2/2 f^{(0)} d^3v/p_B$ (similarly, $\beta_\parallel = m_p\int v_\parallel^2 f^{(0)} d^3v/p_B$), and m_p the proton mass. For a bi-Maxwellian proton distribution, equation (1) reduces to the usual condition [*Vedenov and Sagdeev*, 1959; *Hasegawa*, 1969]

$$\Gamma^* \equiv \beta_\perp\left(\frac{\beta_\perp}{\beta_\parallel} - 1\right) - 1 > 0. \qquad (2)$$

Near threshold ($\Gamma \ll 1$), where it is possible to use a low-frequency, long-wavelength expansion, the growth rate of the mode of wavevector $\mathbf{k}$ is given by

$$\gamma_{\mathbf{k}} = \sqrt{\frac{2}{\pi}}|k_\parallel|\tilde{v}\left(\Gamma - \frac{3}{2}\tilde{r}^2k_\perp^2 - \frac{k_\parallel^2}{k_\perp^2}\chi\right) \qquad (3)$$

where

$$\chi = 1 + \frac{1}{2}(\beta_\perp - \beta_\parallel) \qquad (4)$$

$$\tilde{v}^{-1} = -\sqrt{2\pi}\frac{m_p}{p_B}\int \frac{v_\perp^4}{4}\delta(v_\parallel)\frac{\partial f^{(0)}}{\partial v_\parallel^2}d^3v \qquad (5)$$

$$\tilde{r}^2 = \frac{m_p}{24p_B}\frac{1}{\Omega_p^2}\int\left(-v_\perp^6\frac{\partial f^{(0)}}{\partial v_\parallel^2} - 3v_\perp^4 f^{(0)}\right)d^3v \qquad (6)$$

are assumed to be positive [*Hellinger*, 2007]. The maximum growth rate is given by

$$\gamma_{\rm m} = \frac{1}{4\sqrt{3\pi}}\frac{\tilde{v}}{\tilde{r}}\frac{\Gamma^2}{\chi^{1/2}}, \qquad (7)$$

and appears at $k_{\perp{\rm m}}$ and $k_{\parallel{\rm m}}$ given by

$$k_{\perp{\rm m}}\tilde{r} = \sqrt{\frac{\Gamma}{6}} \quad \text{and} \quad k_{\parallel{\rm m}}\tilde{r} = \frac{1}{2\sqrt{6}}\frac{\Gamma}{\chi^{1/2}}. \qquad (8)$$

For each $(\mathbf{k},\omega)$ mode, the linear response of the distribution function is given by

$$f^{(1)} = \frac{v_\perp}{2}\left(\frac{k_\parallel v_\perp}{k_\parallel v_\parallel - \omega}\frac{\partial f^{(0)}}{\partial v_\parallel} - \frac{\partial f^{(0)}}{\partial v_\perp}\right)\frac{B_z^{(1)}}{B_0}. \qquad (9)$$

In the quasi-linear regime considered by *Shapiro and Shevchenko* [1964], the space-averaged distribution function $\langle f\rangle$ obeys the diffusion equation (in velocity space)

$$\frac{\partial\langle f\rangle}{\partial t} = \sum_{\mathbf{k}}\gamma_{\mathbf{k}}\frac{|B_z^{(1)}(\mathbf{k})|^2}{B_0^2}\mathcal{Q}_{\mathbf{k}}\langle f\rangle \qquad (10)$$

where

$$\begin{aligned}\mathcal{Q}_{\mathbf{k}}\langle f\rangle \;=\; & \frac{1}{4}\left\{\frac{\partial}{\partial v_\parallel}\left(\frac{k_\parallel^2 v_\perp^4}{k_\parallel^2 v_\parallel^2 + \gamma_{\mathbf{k}}^2}\frac{\partial\langle f\rangle}{\partial v_\parallel}\right)\right. \\ & \left. +\; \frac{1}{v_\perp}\frac{\partial}{\partial v_\perp}\left(v_\perp^3\frac{\partial\langle f\rangle}{\partial v_\perp} - \frac{2k_\parallel^2 v_\parallel v_\perp^4}{k_\parallel^2 v_\parallel^2 + \gamma_{\mathbf{k}}^2}\frac{\partial\langle f\rangle}{\partial v_\parallel}\right)\right\},\end{aligned} \qquad (11)$$

supplemented by

$$\frac{\partial B_z^{(1)}(\mathbf{k})}{\partial t} = \gamma_{\mathbf{k}}B_z^{(1)}(\mathbf{k}) \qquad (12)$$

where $\gamma_{\mathbf{k}}$ refers to the instantaneous growth rate defined by equations (1,3–6) with $f^{(0)}$ replaced by $\langle f\rangle$.

3. Numerical schemes for VM Equations

In order to address the nonlinear dynamics of mirror modes, numerical simulations of the VM equations were performed in one space dimension, by assuming variations only along a direction

(parametrized by the coordinate ζ) making a prescribed angle θ with the ambient field (taken in the z-direction), usually corresponding to the largest linear growth rate. In the (ζ, z)-plane, η refers to the direction perpendicular to ζ, and x to the direction perpendicular to z. The direction perpendicular to the (ζ, z)-plane, is parametrized by the coordinate y. Periodic boundary conditions are assumed for the space variable. As already mentioned, both hybrid PIC and Eulerian simulations of VM equations were performed, the two methods appearing as complementary. The former, based on a resolution of the Vlasov equation by the characteristic method, is suitable for integration in large computational domains because of its computational efficiency. The latter, that is usually more accurate but also more time consuming, was implemented in the case of relatively small boxes. This algorithm that is free from statistical noise is especially adapted to simulations close to threshold. Although in this case, the distribution function remains largely unperturbed, a high resolution is nevertheless required in the velocity space in order to make Landau resonances well resolved. Both codes were extensively tested and compared with each other. We checked that the resulting structures are the same, and so are the typical time scales.

3.1. Hybrid PIC Simulations

We used a hybrid code based on *Matthews* [1994] for a proton-electron plasma where electrons are considered as a massless, charge neutralizing fluid, with a constant temperature here taken almost zero, while the protons are described by a particle-in-cell model and are advanced by an implicit leapfrog scheme

$$\frac{\mathbf{v}_{n+1} - \mathbf{v}_n}{\Delta t} = \frac{q}{m}\left[\mathbf{E}_{n+1/2} + \frac{\mathbf{v}_{n+1} + \mathbf{v}_n}{2} \times \mathbf{B}_{n+1/2}\right] \quad (13)$$

that requires the fields to be known at half time steps ahead of the particle velocities, in order to guarantee a better energy conservation. This is achieved by advancing the current density to this time step with only one computational pass through the particle data at each time step. The particle contribution to the current density at the relevant mesh points is evaluated with bilinear weighting followed by smoothing over three points. No smoothing is performed on the electromagnetic fields, and no resistivity is included in Ohm's law. The magnetic field is advanced in time with a modified midpoint method, which allows time substepping for the advance of the field.

A resolution of 1024 points is used for the space variable in both simulations described below. In the former (Section 4.1) the mesh size is $\Delta\zeta = 2d_p$, while in the latter (Section 7) it is $\Delta\zeta = d_p$, where $d_p = v_A/\Omega_p$ is the proton inertial length, defined as the ratio of the Alfvén velocity to the ion gyrofrequency. Such a large computational box enables the system to evolve freely, with negligible finite-size effects. There are initially 500,000 macroparticles per cell, in order to make the numerical noise as low as possible with the available processor array. More specifically, the noise level in one-dimensional particle simulations scaling like the inverse of the particle number per cell, the large number of particles we used is aimed to ensure a good separation between the generated waves and the noise, both for the magnetic fluctuations and the distribution function. Such extremely high number of (macro) particles per cell is not common in hybrid simulations. The evolution of nonlinear structures in cases not too close to threshold can be captured in simulations with a number of particles per cell smaller by three orders of magnitude [*Baumgärtel et al.*, 2003]. In both simulations, the time step for the particle advance is $\Delta t = 0.05/\Omega_p$, whereas the magnetic field $\mathbf{B}$ is advanced with a smaller time step $\Delta t_B = \Delta t/4$.

3.2. The Eulerian Code

This hybrid approach is based on a fluid description of the electrons which, in the present simulations, are assumed at zero temperature (in hybrid PIC simulations, $\beta_e = 10^{-2}$), and on an Eulerian integration scheme for the VM equations. The latter advances the proton distribution function f_p in the 4-dimensional phase space $(\zeta, v_\zeta, v_\eta, v_y)$, using the electromagnetic splitting method proposed in *Mangeney et al.* [2002], where the space and velocity advection terms are advanced separately. This method ensures that there will be no secular growth in the energy conservation error. In particular, the advection equation is solved by using a third order Van Leer scheme. The splitting algorithm is coupled to the Current Advance Method (CAM) introduced in *Matthews* [1994] and extended to the hybrid case in *Valentini et al.* [2007]. Furthermore, by assuming quasi-neutrality and neglecting the displacement current, the electric field is calculated by means of a generalized Ohm's law including electron inertia, while the magnetic field is obtained by solving the Faraday equation.

A computational domain of size $L_\zeta = 15 \times 2\pi\, d_p$ is used, thus smaller than in hybrid PIC simulations. The mesh sizes for the various variables are $\Delta\zeta = 0.73$, $\Delta v_\zeta = \Delta v_\eta = 0.16$, $\Delta v_y = 0.25$.

The initial conditions of all Eulerian simulations presented here are as follows. We assume an ambient homogeneous magnetic field in the form

$$\mathbf{B}_0 = B_0 \cos\theta\, \widehat{\mathbf{e}}_\zeta + B_0 \sin\theta\, \widehat{\mathbf{e}}_\eta \quad (14)$$

and an equilibrium bi-Maxwellian normalized proton distribution function with a temperature anisotropy $A = T_\perp/T_\parallel$, given by

$$f^{(0)} = \frac{1}{\pi^{3/2} v_{th\parallel} v_{th\perp}^2} \exp\Big\{ - \frac{1}{v_{th\perp}^2}\Big[(\sin^2\theta + A\cos^2\theta)u_\zeta^2 + (\cos^2\theta + A\sin^2\theta)u_\eta^2 + (A-1)\sin 2\theta\, u_\zeta u_\eta + u_y^2\Big]\Big\}, \quad (15)$$

where $v_{th\perp} = (2T_\perp/m_p)^{1/2}$ and $v_{th\parallel} = (2T_\parallel/m_p)^{1/2}$ are the proton perpendicular and parallel thermal velocities respectively. We consider two different types of initial perturbations. The first one corresponds to density and magnetic fluctuations given by

$$\delta f = \mu_1 \sum_{m=1}^{N_m} \cos(2\pi m\zeta/L_\zeta + \phi_m)/m \quad (16)$$

$$\delta B_\eta = \mu_2 \sum_{l=1}^{N_l} \cos(2\pi l\zeta/L_\zeta + \phi_l)/l, \quad (17)$$

where μ_1 and μ_2 are small coefficients, usually taken equal to 10^{-3}. The phases ϕ_m and ϕ_l are randomly chosen. The second one consists in an initial magnetic hole or hump without density fluctuations, and corresponds to

$$\delta f = 0 \quad (18)$$

$$\delta B_\eta = \pm a\,(\tanh^2[(\zeta - \zeta_0)/L_h] - 1), \quad (19)$$

where the amplitude a is usually taken equal to 0.5 and the width L_h to 5. The structure is centered in the computational box by choosing $\zeta_0 = L_\zeta/2$. The positive sign corresponds to a magnetic depression and the negative one to a bump like perturbation.

4. Simulations Near Threshold

Simulations were performed both in an extended domain and in a relatively small computational box, in order to address the possible influence of finite-size effects. As discussed below, such effects can for example prevent the development of a quasi-linear regime and enhance magnetic energy oscillations due to trapping. As previously mentioned, different algorithms appear suitable in these different configurations.

4.1. Dynamics in an Extended Domain

These simulations were done using the hybrid PIC algorithm. The system evolves from a bi-Maxwellian proton distribution function with an inherent numerical noise. The initial proton parameters

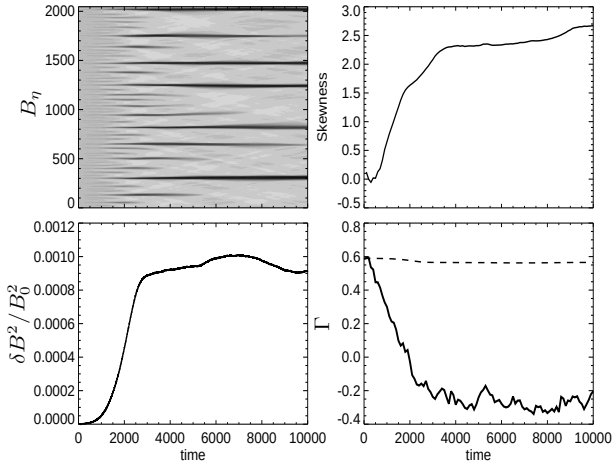

Figure 1. Simulation of the mirror instability in an extended domain near threshold ($\beta_\parallel = 1$, $T_\perp/T_\parallel = 1.857$, $\theta = 72.8^\circ$). Gray scale plot of the magnetic fluctuation B_η as a function of time and space (left top); Time evolution of skewness of B_η (right top), of fluctuating magnetic energy $\delta B^2/B_0^2$ (left bottom), of the instantaneous distance from the threshold (right bottom): Γ (solid line) as given by equation (1) and the corresponding bi-Maxwellian value Γ^* (dashed line) obtained from equation (2).

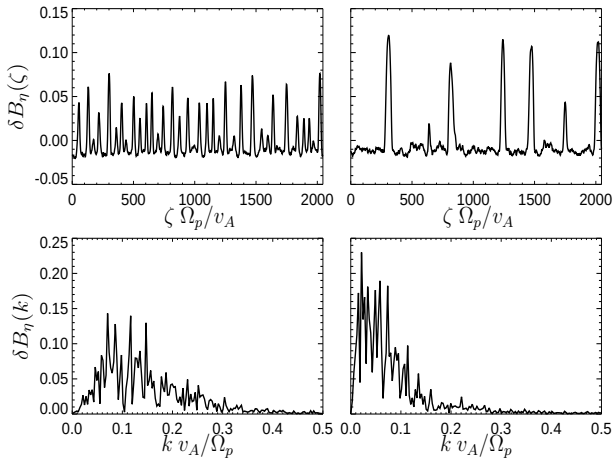

Figure 2. Same conditions as Figure 1. Profile (top) and spectrum (bottom) of δB_η at times $t = 2000/\Omega_p$ (left) and $t = 10000/\Omega_p$ (right).

are $\beta_\parallel = 1$ and $\beta_\perp = 1.857$, whereas the electrons are cold with $\beta_e = 10^{-2}$. For these parameters, $\Gamma = 0.6$, and the full kinetic linear theory predicts a maximum growth rate $\gamma = 5 \cdot 10^{-3}\Omega_p$ for a wavenumber direction making an angle $\theta = 72.8^\circ$ with the ambient field. Note that the asymptotic expression, given in section 2, predicts $\gamma_m = 10^{-2}\Omega_p$. These parameters result from a compromise between numerical constraints and the aim to be as close as possible to threshold. The integration being performed in a large domain (of size $2048\ d_p$), a broad range of modes is linearly unstable, even relatively close to threshold. Simulations were also performed with $\beta \sim 1$, leading to a qualitatively similar dynamics. We however concentrate here on cold electrons, a regime permitting an easier comparison with the theory that becomes more complex when the electrons are warm.

Figure 1 (top left) displays the gray scale plot of the amplitude B_η of magnetic fluctuations, as a function of time and space. Coherent structures in the form of magnetic humps are seen to emerge relatively early. As time elapses, they exhibit a coarsening process leading to the persistence at the end of the simulation of only a few intense and well-separated magnetic peaks, in agreement with previous simulations by *Baumgärtel et al.* [2003]. In order to quantify the onset of the structures and their typical profile, we plot in Figure 1 (top right) the skewness of the magnetic fluctuations B_η, that starts around zero, rapidly increases within the period 600–$3000\,\Omega_p^{-1}$ and saturates at a value exceeding 2.5. The period of the rapid growth coincides with that of intensive coarsening, and the evolution to a significant positive value is consistent with the formation of strong magnetic humps.

The energy of magnetic fluctuations (Figure 1, left bottom) first increases monotonically until $3000\,\Omega_p^{-1}$ when it rapidly saturates. Later on, both the skewness and the fluctuation energy display only weak variations on long time scales, associated with the slowing down of the coarsening effect. Figure 2 illustrates typical stages of this evolution by displaying the profiles of magnetic fluctuations B_η (top) and their Fourier spectra (bottom) at time $t = 2000\,\Omega_p^{-1}$

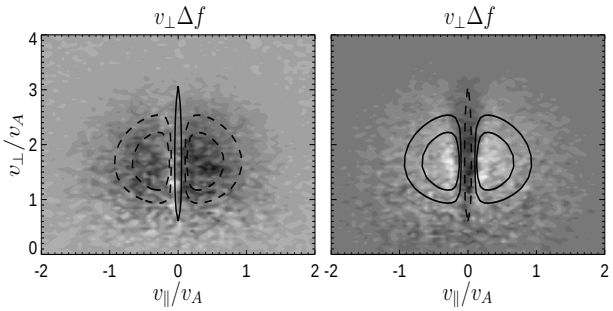

Figure 3. Same conditions as Figure 1. Gray scale plots of $v_\perp \Delta f$ averaged over regions where $\delta B_\eta/B_0 > 0.01$ (left panel) and $\delta B_\eta/B_0 < -0.01$ (right panel), at time $t = 1000/\Omega_p$. White corresponds to positive values and black to negative ones. Superimposed are the contours of the linear prediction, $v_\perp f^{(1)}$, at maximum (left) and, symmetrically, minimum (right) of $B_z^{(1)}$, for the most unstable mode. Solid and dashed lines denote positive and negative values of $v_\perp f^{(1)}$, respectively.

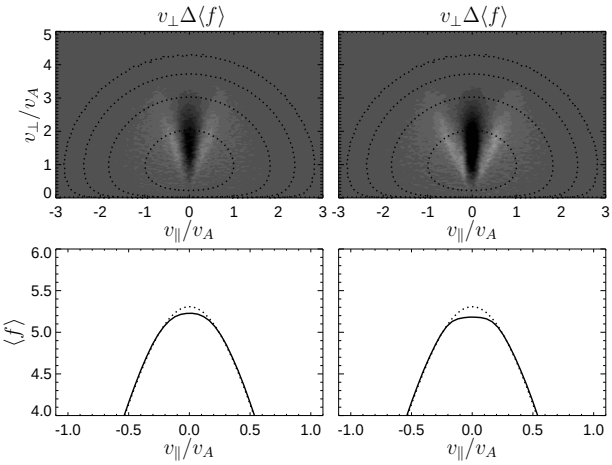

Figure 4. Same conditions as Figure 1. Simulation results at times $t = 2000/\Omega_p$ (left panels) and $t = 10,000/\Omega_p$ (right panels): (top panels) Gray scale plots of the proton distribution variation $v_\perp \Delta\langle f\rangle$ (black corresponds to negative values and white to positive ones). Dotted lines correspond to the contours of the initial condition $v_\perp f^{(0)}$. (bottom panels) Profiles (solid line) of the proton distribution function $\langle f\rangle$ integrated over $v_\perp$, together with the initial profile (dotted line).

(left) during the period of active coarsening and at the later time $t = 10000\,\Omega_p^{-1}$ of the simulation (right).

It is also of interest to analyze the global evolution of the plasma in terms of the instantaneous distance to the instability threshold. Figure 1 (right bottom) shows the time evolution of this distance Γ (solid line) given by equation (1) with $f^{(0)}$ replaced by the space-averaged instantaneous proton distribution function. Dashed line corresponds to the bi-Maxwellian expression Γ^* calculated from equation (2) with the instantaneous parallel and perpendicular betas. A main observation is that Γ rapidly departs from Γ^* (that hardly changes) and displays a monotonic decrease, becoming negative (at $t \approx 2000\,\Omega_p^{-1}$), while the energy of the magnetic fluctuations is still growing. It saturates by $3000\,\Omega_p^{-1}$, at about the same time as the skewness and the energy of the magnetic fluctuations. The very different behavior of Γ and Γ^* indicates a significant distortion of the proton distribution function during the evolution. In order to make this observation more quantitative, let Δf denote the difference between the proton distribution function at times t and 0. Figure 3 displays as gray scale plots the averaged value of $v_\perp \Delta f$ over regions where $\delta B_\eta / B_0 > 0.01$ (left panel) and $\delta B_\eta / B_0 < -0.01$ (right panel), at time $t = 1000\,\Omega_p^{-1}$ which roughly corresponds to the end of the linear phase. During this period, the variation can be estimated by the linear response of the distribution function $f^{(1)}$ given by equation (9). On Figure 3, we thus superimpose the contours of $v_\perp f^{(1)}$ at maximum (left) and, symmetrically, minimum (right) value of $B_z^{(1)}$ for the linearly most unstable mode. These extrema are supposed to mimic the high and low regions of δB_η. Solid and dashed curves denote positive and negative values of $v_\perp f^{(1)}$, respectively. We observe that at maximum (minimum) of δB_η the density of resonant particles (with $v_\parallel \sim 0$) increases (decreases), whereas the density of non-resonant particles decreases (increases) in good agreement with the linear prediction. Note that the noisy aspect of the distribution function perturbation in magnetic humps is due to the poorer statistics in these regions. These results are consistent with the schematic Figure 2 of *Southwood and Kivelson* [1993] and similar to the simulation results displayed in Figure 1 (top) of *Pantellini et al.* [1995].

A main question concerns the detailed nonlinear processes leading to the saturation of the linear instability, and their signature at the level of the ion distribution function. Using a gray scale plot where here white corresponds to negative values whereas black to positive ones, Figure 4 (top) indeed reveals important modifications of the space-averaged proton distribution function as measured by $v_\perp \Delta\langle f\rangle$, where $\Delta\langle f\rangle = \langle f\rangle - f^{(0)}$ at two different times $t = 2000/\Omega_p$ (left) and $t = 10,000/\Omega_p$ (right). The significant changes mainly affect the resonant particles (with $v_\parallel \sim 0$). The two bottom panels of the figure show at these two times the profiles (solid line) of $\langle f\rangle$ integrated over $v_\perp$, together with the corresponding initial profiles (dotted line). The visible flattening of the distribution profile is confirmed by detailed analysis of its behavior near $v_\parallel = 0$, which shows that it is not parabolic in $v_\parallel$ and consistent with $\partial\langle f\rangle/\partial v_\parallel^2 \sim 0$.

This evolution of the distribution function can be plausibly interpreted in terms of a diffusion in velocity space, as predicted by the

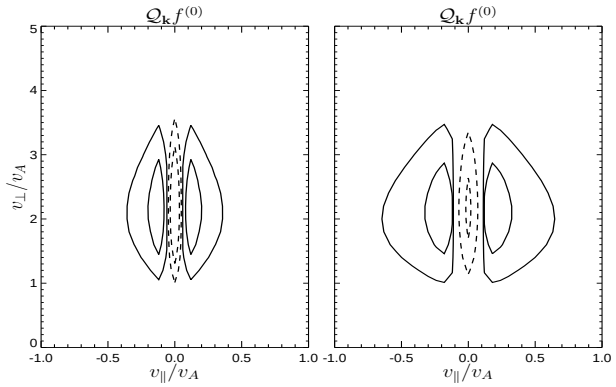

Figure 5. Schematic view of the prediction of the quasi-linear theory: Effect of the diffusion operator on the initial proton distribution function $\mathcal{Q}_{\mathbf{k}} f^{(0)}$ for the most unstable mode (left) and for a weakly unstable mode (right). Solid (dashed) contours show positive (negative) values.

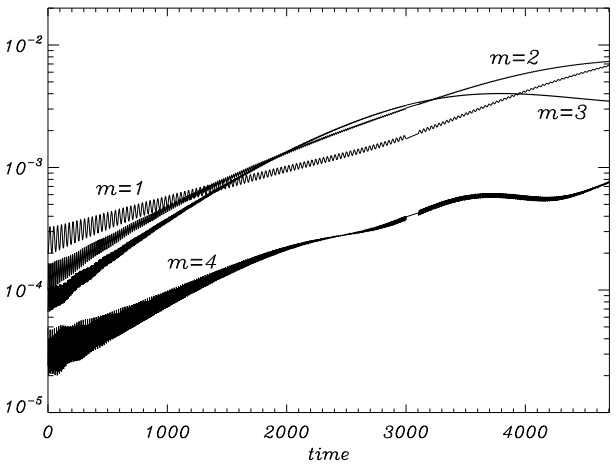

Figure 6. Time evolution of unstable modes in an Eulerian simulation very near threshold ($\beta_\parallel = 6$, temperature anisotropy $T_\perp/T_\parallel = 1.25$, with $\theta = 83.86°$).

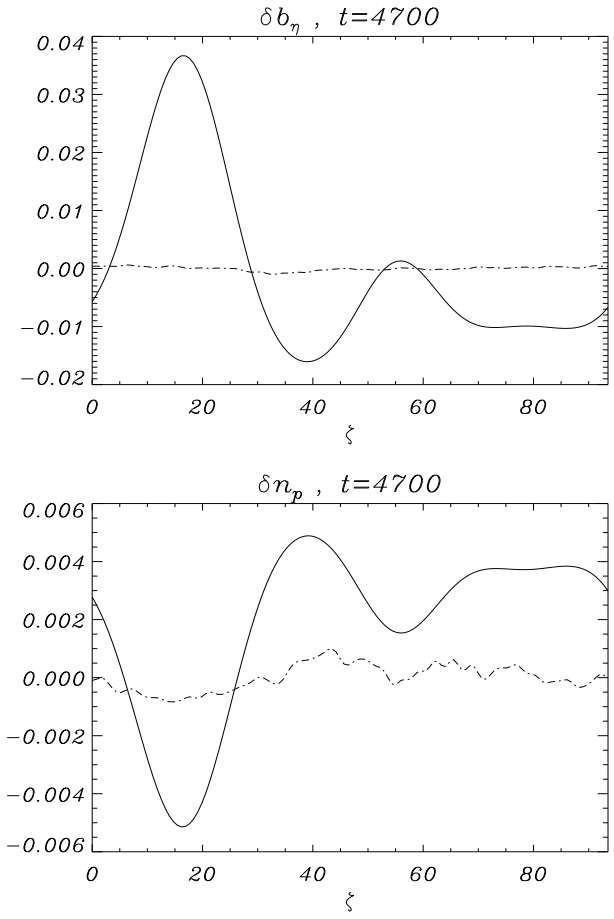

Figure 7. Magnetic humps and density holes formed as the development of the mirror instability presented in Figure 6. Here and in the following figures displaying results of the Eulerian simulations, dashed lines refer to initial conditions and solid lines to the final time of the simulations.

quasi-linear theory. To address this question it would be necessary to resolve numerically the full quasi-linear system (Section 2). This project is beyond the scope of this paper. Here we limit ourselves to qualitatively estimate the effect of quasi-linear diffusion by calculating $\mathcal{Q}_{\mathbf{k}} f^{(0)}$ (defined by equation (11)). Figure 5 shows the results of this calculation for the most unstable (left) and a weakly unstable (right) modes. Solid and dashed curves denote positive and negative values of $\mathcal{Q}_{\mathbf{k}} f^{(0)}$, respectively. We see that the quasi-linear theory predicts a preferable diffusion of particles with small parallel velocity to regions with higher parallel velocity, in qualitative agreement with the simulation results (Figure 4, top).

These results lead to the conclusion that in an extended domain near threshold, a quasi-linear regime can exist during the early nonlinear phase. However, later on, the onset of coherent structures invalidates the random phase approximation of the quasi-linear theory. Furthermore, as previously noted on Figure (1, bottom right), the energy of the magnetic fluctuations continues to increase even when the system is linearly stable, an effect which is also at variance with the quasi-linear theory.

The further evolution thus requires a different theoretical approach, more suitable for describing the dynamics of coherent nonlinear waves (see Section 5.1). Moreover, as already mentioned, the quasi-linear regime that assumes an incoherent dynamics where the phase of the various modes can be viewed as essentially random, requires a large number of interacting modes and thus a large computational box. As discussed in the next section, this transient is indeed absent in a small computational domain where, after the linear phase, the system directly enters a regime of structure formation.

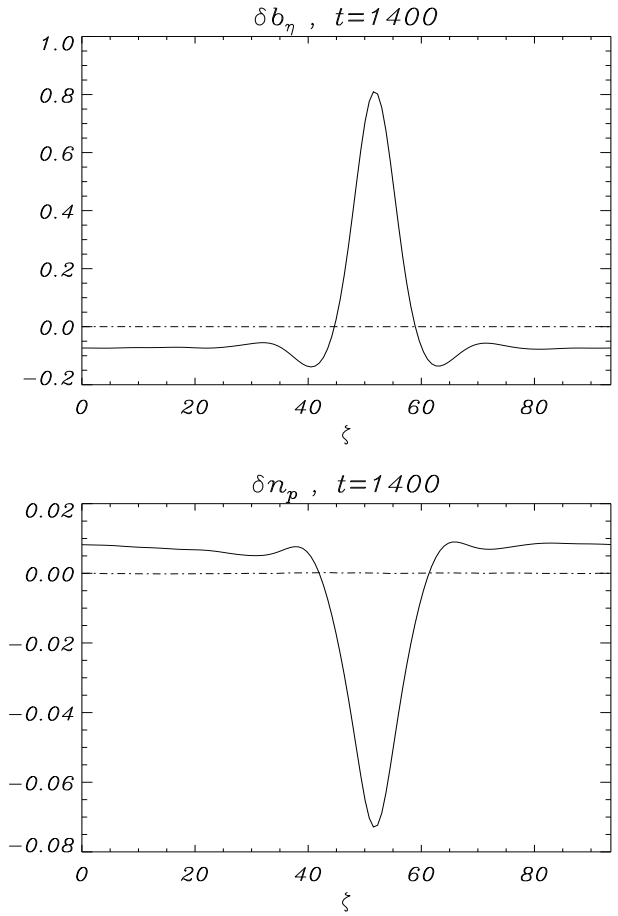

Figure 8. Magnetic and density fluctuation profiles at initial and final times of the simulation, in the case $T_\perp/T_\parallel = 1.4$, $\beta_\parallel = 15$ and $\theta = 78.53^\circ$.

4.2. Dynamics in a Small Computational Domain

As a first run (based on a Eulerian scheme) performed in a small computational box, we consider a condition close to threshold, namely $\beta_\parallel = 6$, $\theta = 83.86^\circ$ and $T_\perp/T_\parallel = 1.25$. The run is initialized with a weak random noise as indicated in Section 3.2. Figure 6 displays the time evolution of the linearly unstable modes and their nonlinear saturation. The most unstable mode ($m = 3$) has a growth rate $1.7 \cdot 10^{-3}$, which compares well with the value $2 \cdot 10^{-3}$ computed from the full kinetic theory. In spite of its relatively small value, it significantly differs from the asymptotic prediction $\gamma_m = 3.6 \cdot 10^{-2}$ (see Section 2), since in the conditions of the simulation $\Gamma = 0.88$ initially. Here also the possibility of performing simulations very close to threshold is limited by numerical resources. In physical space, the evolution leads to the formation of a steady magnetic hump with an anticorrelated density hole (Figure 7). In this simulation in a small domain, which involves a very low numerical noise, no flattening is visible on the distribution function, even at short times, consistent with the absence of a quasi-linear dynamics.

Large values of the beta parameter were also observed in space plasmas. For example, *Soucek et al.* [2008] report values of $\beta_\parallel = 14$ and *Leckband et al.* [1995] mention instances with $\beta = 30$ in the terrestrial magnetosheath. A second simulation was thus performed at larger distance from threshold by taking $\beta_\parallel = 15$ and $T_\perp/T_\parallel = 1.4$ with $\theta = 78.53^\circ$, which corresponds to $\Gamma = 7.4$. Essentially the same dynamics is observed, with nevertheless the formation of structures with much larger amplitudes (Figure 8). It is noticeable that in contrast with the dynamics in a large computational domain, the energy of magnetic fluctuations displays time oscillations whose amplitude is progressively damped, suggesting the relaxation to a steady nonlinear structure. This effect is shown in Figure 9 that displays the grey scale plot of the magnetic fluctuations B_η as a function of space and time (top) and the time evolution of the magnetic-energy fluctuations $\delta B^2/B_0^2$ (bottom). This effect is in fact a consequence of the size of the domain, and not

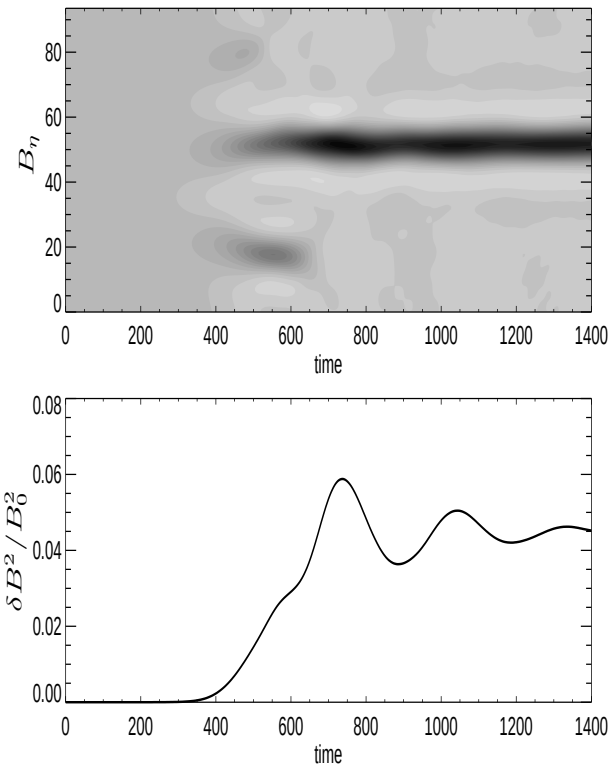

Figure 9. Grey scale plot of the magnetic fluctuations B_η as a function of space and time and time evolution of the magnetic-energy fluctuations $\delta B^2/B_0^2$ in the conditions of Figure 8.

of the distance from threshold. Indeed, a PIC simulation with the same physical parameters as that reported in Figure 1 but performed in a small box displays the same type of oscillations. In both cases, their period is consistent with the ion bounce time $T = 2\pi/\omega_{\rm tr}$, where $\omega_{\rm tr}^2 = (1/2)v_{th_\perp}^2 k_\parallel^2(\delta B/B_0)$, suggesting that particle trapping is at the origin of this effect. We also note on Figure 9 (top) that, in addition to the main structure, a weaker one is visible during the time interval $400 < t < 600$. Afterwards, it is subject to corsening. A signature of this effect is conspicuous on the time vatiation of the magnetic-energy fluctuations near $t = 600$.

5. Reductive Perturbative Expansion Near Threshold

5.1. Asymptotic Theory

Near threshold, the onset of coherent structures is amenable to an asymptotic approach based on the remark that, in this limit, linearly unstable modes are located at large scales. This approach, implemented in *Kuznetsov et al.* [2007a] by patching the linear kinetic theory with an estimate of the nonlinear effects in the framework of the drift-kinetic equation, is here revisited using a systematic reductive perturbative expansion directly performed on the VM equations.

The equation for the mean proton velocity, as classically derived from the Vlasov equation, reads

$$\frac{d\mathbf{u}}{dt} + \frac{1}{\rho}\boldsymbol{\nabla}\cdot\mathbf{p} - \frac{e}{m_p}(\mathbf{E} + \frac{1}{c}\mathbf{u}\times\mathbf{B}) = 0, \tag{20}$$

where, for cold and massless electrons,

$$\mathbf{E} = -\frac{1}{c}\Big(\mathbf{u} - \frac{\mathbf{j}}{ne}\Big)\times\mathbf{B}, \tag{21}$$

with $\mathbf{j} = (c/4\pi)\boldsymbol{\nabla}\times\mathbf{B}$. The ion pressure tensor is rewritten as the sum of gyrotropic and gyroviscous contributions $\mathbf{p} = p_\perp\mathbf{n} + p_\parallel\boldsymbol{\tau} + \boldsymbol{\Pi}$, with $\mathbf{n} = \mathbf{I} - \widehat{\mathbf{b}}\otimes\widehat{\mathbf{b}}$ and $\boldsymbol{\tau} = \widehat{\mathbf{b}}\otimes\widehat{\mathbf{b}}$, where $\widehat{\mathbf{b}} = \mathbf{B}/|B|$ is the unit vector along the local magnetic field. Equation (20) is then rewritten in the form

$$\begin{aligned}\rho\frac{d\mathbf{u}}{dt} &= -\boldsymbol{\nabla}\Big(p_\perp + \frac{|B|^2}{8\pi}\Big)\\ &+\Big(1 + \frac{4\pi}{|B|^2}(p_\perp - p_\parallel)\Big)\frac{\mathbf{B}\cdot\boldsymbol{\nabla}\mathbf{B}}{4\pi}\\ &\quad -\widehat{\mathbf{b}}\frac{|B|^2}{4\pi}(\widehat{\mathbf{b}}\cdot\boldsymbol{\nabla})\Big(1 + \frac{4\pi}{|B|^2}(p_\perp - p_\parallel)\Big) - \boldsymbol{\nabla}\cdot\boldsymbol{\Pi}.\end{aligned} \tag{22}$$

Projecting this equation on the plane perpendicular to the local magnetic field then gives

$$\begin{aligned}\mathbf{n}\cdot\rho\frac{d\mathbf{u}}{dt} &= -\boldsymbol{\nabla}\Big(p_\perp + \frac{|B|^2}{8\pi}\Big)\\ &+\Big(1 + \frac{4\pi}{|B|^2}(p_\perp - p_\parallel)\Big)\frac{(\mathbf{B}\cdot\boldsymbol{\nabla})\mathbf{B}}{4\pi}\\ &+(\mathbf{B}\cdot\boldsymbol{\nabla})\Big(p_\perp + \frac{|B|^2}{8\pi}\Big)\frac{\mathbf{B}}{|B|^2}\\ &-\Big(1 + \frac{4\pi}{|B|^2}(p_\perp - p_\parallel)\Big)(\mathbf{B}\cdot\boldsymbol{\nabla})\Big(\frac{|B|^2}{2}\Big)\frac{\mathbf{B}}{4\pi|B|^2} - \mathbf{n}\cdot\boldsymbol{\nabla}\cdot\boldsymbol{\Pi}.\end{aligned} \tag{23}$$

In order to address the asymptotic regime, we rescale the independent variables in the form $X = \sqrt{\varepsilon}x$, $Y = \sqrt{\varepsilon}y$, $Z = \varepsilon z$, $T = \varepsilon^2 t$, where ε measures the distance to threshold, and expand any field φ in the form

$$\varphi = \sum_{n=0}^{\infty}\varepsilon^{n/2}\varphi_{n/2}, \tag{24}$$

as indicated in Appendix A. At this step, a remark is in order. The ion bounce frequency in a structure of size ε^{-1} is of order $\varepsilon^{3/2}$ [*Pantellini et al.*, 1995], suggesting a time scale $\varepsilon^{-3/2}$ for the flattening of the distribution function near the zero parallel velocity. This time scale thus appears shorter than the one assumed by the performed scaling. As discussed later, this flattening process turns out to have a negligible effect on the nonlinear dynamics during the considered time scale.

When retaining the two first nontrivial orders, we get ($\boldsymbol{\nabla}_\perp = (\partial_X, \partial_Y)$ denoting the transverse gradient)

$$\begin{aligned}&\boldsymbol{\nabla}_\perp\Big(p_\perp^{(1)} + \frac{B_0 B_z^{(1)}}{4\pi}\Big)\\ &+\varepsilon\Big\{\boldsymbol{\nabla}_\perp\Big(p_\perp^{(2)} + \frac{B_0 B_z^{(2)}}{4\pi} + \frac{(B_z^{(1)})^2}{8\pi}\Big)\\ &-\frac{2}{\beta_\perp}\Big(1 + \frac{\beta_\perp - \beta_\parallel}{2}\Big)p_\perp^{(0)}\partial_Z\Big(\frac{\mathbf{B}_\perp^{(3/2)}}{B_0}\Big)\\ &+\boldsymbol{\nabla}_\perp\cdot\boldsymbol{\Pi}_\perp^{(2)} + \partial_Z\boldsymbol{\Pi}_{\perp Z}^{(3/2)}\Big\} = O(\varepsilon^2),\end{aligned} \tag{25}$$

that expresses the condition of pressure balance.

The condition $\boldsymbol{\nabla}_\perp\times\mathbf{B}_\perp^{(3/2)} = 0$ established in Appendix B, together with the divergenceless condition $\boldsymbol{\nabla}_\perp\cdot\mathbf{B}_\perp^{(3/2)} + \partial_Z B_z^{(1)} = 0$, implies

$$\mathbf{B}_\perp^{(3/2)} = (-\Delta_\perp)^{-1}\boldsymbol{\nabla}_\perp\partial_Z B_z^{(1)}. \tag{26}$$

Here, the subscript $\perp$ refers to vector component perpendicular to the ambient field (taken along z). Defining $b_z = B_z^{(1)} + \varepsilon B_z^{(2)}$ and $\overline{p}_\perp = p_\perp{}^{(1)} + \varepsilon p_\perp^{(2)}$, we can write at the order of the expansion

$$\begin{aligned}&\boldsymbol{\nabla}_\perp\Big[\overline{p}_\perp + \frac{B_0}{4\pi}b_z\\ &+\varepsilon\frac{b_z^2}{8\pi} + \frac{2\varepsilon}{\beta_\perp}\Big(1 + \frac{\beta_\perp - \beta_\parallel}{2}\Big)p_\perp^{(0)}(\Delta_\perp)^{-1}\partial_{ZZ}\frac{b_z}{B_0}\Big]\\ &+\varepsilon\Big(\boldsymbol{\nabla}\cdot\boldsymbol{\Pi}\Big)_\perp^{(5/2)} = O(\varepsilon^2),\end{aligned} \tag{27}$$

where the last term in the LHS, given by equation (C9), is also a transverse gradient.

Using equations (C2) and (C9) to express the perpendicular pressure and the gyroviscous force and rewriting $B_0^2/8\pi = p_\perp^{(0)}/\beta_\perp$, we obtain in the case of a bi-Maxwellian equilibrium ion distribution function

$$\begin{aligned}&-\beta_\perp\Big(\frac{\beta_\perp}{\beta_\parallel} - 1 - \frac{1}{\beta_\perp}\Big)\frac{B_0 b_z}{4\pi}\\ &+\varepsilon\frac{\sqrt{\pi}}{v_{th\,\parallel}}\Big(-\mathcal{H}\,\partial_Z\Big)^{-1}\partial_T\frac{\beta_\perp^2}{\beta_\parallel}\frac{B_0 b_z}{4\pi}\\ &-\varepsilon p_\perp^{(0)}\Big[\frac{9}{4\beta_\perp}r_L^2\Delta_\perp\frac{b_z}{B_0}\\ &+\Big(1 - 4\frac{\beta_\perp}{\beta_\parallel} + 3\Big(\frac{\beta_\perp}{\beta_\parallel}\Big)^2\Big)\Big(\frac{b_z}{B_0}\Big)^2\Big]\\ &+\varepsilon\frac{b_z^2}{8\pi} + \varepsilon\Big(2 - \frac{\beta_\parallel}{\beta_\perp}\Big)p_\perp^{(0)}\Delta_\perp^{-1}\partial_{ZZ}\frac{b_z}{B_0}\\ &-\frac{3}{4}\varepsilon\Big(1 - \frac{\beta_\perp}{\beta_\parallel}\Big)p_\perp^{(0)}r_L^2\Delta_\perp\frac{b_z}{B_0} = O(\varepsilon^2).\end{aligned} \tag{28}$$

We note that the time derivative and the Hilbert transform $\mathcal{H}$ originate from Landau resonance. The parameter $r_L = v_{th\perp}/\Omega_p$ is the ion Larmor radius. The two nonlinear terms, when put together, involve a coefficient λ that simplifies when noticing that it can be evaluated by neglecting the distance to threshold, thus mak-

ing the replacement $\beta_\perp/\beta_\parallel = 1 + 1/\beta_\perp$. This gives

$$\lambda = 1 - 4\frac{\beta_\perp}{\beta_\parallel} + 3\Big(\frac{\beta_\perp}{\beta_\parallel}\Big)^2 + \frac{1}{\beta_\perp} = \frac{3}{\beta_\perp}\Big(1 + \frac{1}{\beta_\perp}\Big). \quad (29)$$

We thus obtain the asymptotic equation governing the nonlinear dynamics of mirror modes near the instability threshold in the form

$$\partial_T \frac{b_z}{B_0} = \frac{v_{th\,\parallel}}{\sqrt{\pi}}\frac{\beta_\parallel}{\beta_\perp}\Big(-\mathcal{H}\partial_Z\Big)\Big\{\frac{1}{\varepsilon}\Big(\frac{\beta_\perp}{\beta_\parallel} - 1 - \frac{1}{\beta_\perp}\Big)\frac{b_z}{B_0} + \frac{3}{4\beta_\perp} r_L^2 \Delta_\perp \frac{b_z}{B_0} - \frac{1}{\beta_\perp}\Big(1 + \frac{\beta_\perp - \beta_\parallel}{2}\Big)\Delta_\perp^{-1}\partial_{ZZ}\frac{b_z}{B_0} - \frac{3}{2}\Big(\frac{1+\beta_\perp}{\beta_\perp^2}\Big)\Big(\frac{b_z}{B_0}\Big)^2\Big\} = O(\varepsilon). \quad (30)$$

This equation can be viewed as the linear dispersion relation of large-scale mirror modes retaining leading order FLR corrections, supplemented by dominant nonlinear contributions. It is noticeable that kinetic effects (such as Landau and FLR effects) contribute only linearly.

We now define $\chi = 1 + (\beta_\perp - \beta_\parallel)/2$ and characterize the regime of linear stability or instability by the parameter $\sigma = \mathrm{sgn}(\beta_\perp/\beta_\parallel - 1 - 1/\beta_\perp)$. The expansion parameter ε is related to the distance to threshold by the condition $|\beta_\perp/\beta_\parallel - 1 - 1/\beta_\perp| = \varepsilon\chi/\beta_\perp$, or in other words $\varepsilon = \Gamma^*/\chi$ with Γ^* defined in equation (2) as the bi-Maxwellian threshold parameter. We then perform a simple rescaling by introducing the new longitudinal and transverse coordinates $\xi = (2/\sqrt{3})\chi^{1/2} r_L^{-1} Z$, $\mathbf{R'}_\perp = (2/\sqrt{3})\chi^{1/2} r_L^{-1}\mathbf{R}_\perp$, and the new time variable $\tau = (2/\sqrt{3})(\sqrt{\pi}\beta_\perp)^{-1}(\chi\beta_\parallel/\beta_\perp)^{3/2}\Omega_p T$. We also write

$$b_z/B_0 = 2\chi\beta_\perp\,(1+\beta_\perp)^{-1}\,U. \quad (31)$$

The equation then reduces to

$$\partial_\tau U = -\mathcal{H}\partial_\xi\Big[\sigma U + \Delta_\perp U - \Delta_\perp^{-1}\partial_{\xi\xi}U - 3U^2\Big], \quad (32)$$

up to corrections of order ε.

Equation (32) further simplifies when the spatial variations are limited to a direction making a fixed angle with the ambient magnetic field. After a simple rescaling, one gets

$$\partial_T U = \widehat{K}_\Xi\left[(\sigma + \partial_{\Xi\Xi})\,U - 3U^2\right], \quad (33)$$

where Ξ is the coordinate along the direction of variation and $K_\Xi = -\mathcal{H}\partial_\Xi$ is a positive operator whose Fourier transform reduces to the multiplication by the wavenumber absolute value.

Equation (32) possesses the remarkable property of being of the form

$$\partial_T U = -\widehat{K}_Z \delta F/\delta U, \quad (34)$$

where $F = \int\left[-\frac{\sigma}{2}U^2 + \frac{U}{2}\Delta_\perp^{-1}\partial_{ZZ}U + \frac{1}{2}(\nabla_\perp U)^2 + U^3\right]d^3R$ has the meaning of a free energy or a Lyapunov functional. This quantity can only decrease in time [*Kuznetsov et al.*, 2007a].

A main property of equation (32) is the onset of a finite-time singularity, for arbitrary initial conditions when $\varepsilon > 0$ and under the assumption that they are large enough when $\varepsilon < 0$. Near blowup, F is negative and dominated by the $\int U^3 d^3R$ contribution that can be viewed as proportional to the skewness of the magnetic fluctuations. This indicates that blowup solutions of the asymptotic equation (33) take the form of magnetic holes. This property should however be taken with caution because, unless possibly extremely close to threshold (a regime almost impossible to achieve in simulations and insufficiently generic to be relevant for spatial observations), the involved scalings lead to an early breakdown of the asymptotics. Specifically, the size of the structures should be much larger than the ion Larmor radius, in order to make nonlinear FLR corrections irrelevant. In fact, the singularity essentially appears as the signature of a subcritical bifurcation (addressed in detail in *Kuznetsov et al.* [2007b]) where the hydrodynamic nonlinearities enhance the instability, leading to finite-amplitude solutions where neglected contributions, such as the nonlinear kinetic effects, become relevant. As discussed below, nonlinear kinetic effects do not just provide a local smoothing of the singularity but, especially above threshold, prevent the formation of magnetic holes driven by the hydrodynamic nonlinearities. This suggest that the origin of the observed magnetic holes is more complex. A few scenari are discussed in Sections 6 and 7.

5.2. Beyond the Asymptotics: Saturation by Nonlinear FLR Effects

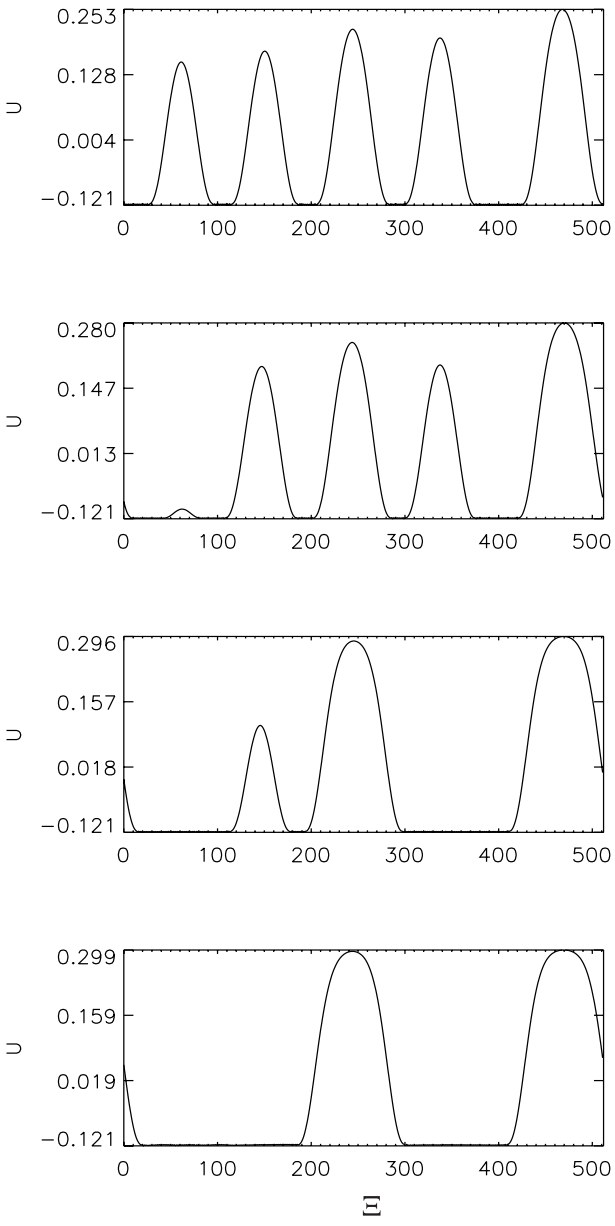

Figure 10. Time evolution of magnetic structures resulting from the mirror instability in the framework of the phenomenological model for $\alpha = 1.54$, $\nu = 10^{-2}$ and a weak initial noise. Panels are displayed at times $t = 3$, 5, 9, and 10 (from top to bottom). The horizontal axis refers to grid point numbers.

Retaining the saturating effects of nonlinear kinetic phenomena is not possible within a rigorous asymptotics but their effects can nevertheless be described phenomenologically. Models previously suggested in order to interpret the nonlinear saturation of the mirror instability were based on the cooling of a population of trapped particles, neglecting FLR corrections [*Kivelson and Southwood*, 1996; *Pantellini*, 1998]. These models mainly explain the formation of deep stationary magnetic holes, while, as seen in Section 2, Vlasov simulations of the mirror instability lead to the formation of magnetic humps above threshold. They also do not reproduce the phenomenon of bistability. A more quantitative, although still phenomenological description was recently suggested by *Pokhotelov et al.* [2007], assuming a flattening of the equilibrium ion distribution function on a range that extends with the wave amplitude. This correction, that tends to reduce the Landau damping, results in a renormalization of the time derivative in equation (33) by a factor that depends on the wave amplitude and reduces to unity in the zero amplitude limit. The leading order correction arising in this factor scales like $U^{1/2}$, consistent with a bounce time scaling like $U^{-3/2}$. This correction, aimed to model the effect of ion particle bouncing, is nevertheless a subdominant term that does not significantly affect the dynamics on the time scale of the present asymptotics.

It turns out that a different saturating process that affect the geometry of the structures can be phenomenologically supplemented to the above asymptotic equation by retaining the local variation of the ion Larmor radius r_L, making the resulting model consistent with VM simulations [*Kuznetsov et al.*, 2007a]. The argument is that in regions of weaker magnetic field (and/or large $T_\perp$), the ion Larmor radius is larger, making stabilizing effects of FLR corrections more efficient than in the linear regime. Consequently, the mirror instability is more easily quenched in magnetic field minima than in maxima, making magnetic humps more likely to form in the saturating phase of the mirror instability.

More quantitatively, due to the conservation of the magnetic moment, the ion Larmor radius satisfies $r_L^2 \propto T_\perp/|B|^2 \propto 1/|B| \approx 1/B_z$. Its variation can be retained in equation (32) by replacing the term $\Delta_\perp U$ by $[1/(1+\alpha U)]\Delta_\perp U$, where α, given by equation (36) below, results from the rescaling procedure. In addition to the Laplacian, which originates from the leading order expansion of a nonlocal operator associated with FLR corrections [*Pokhotelov et al.*, 2005], it is possible to add the next order contribution in the form $(4/9)[\nu/(1+\alpha U)^2]\Delta_\perp^2 U$. This extra term quantitatively improves the model predictions, in that it prevents the formation of regions of very low magnetic field. On the other hand, higher order terms do not drastically affect the value of magnetic field minima $B_{\min} = B_0(1+\alpha U_{\min})$. The model equation that was numerically integrated then reads

$$\partial_T U = \widehat{K}_\Xi \left[\sigma U - 3U^2 + \frac{\partial_\Xi^2 U}{1+\alpha U} - \frac{4\nu\, \partial_\Xi^4 U}{9(1+\alpha U)^2} \right], \quad (35)$$

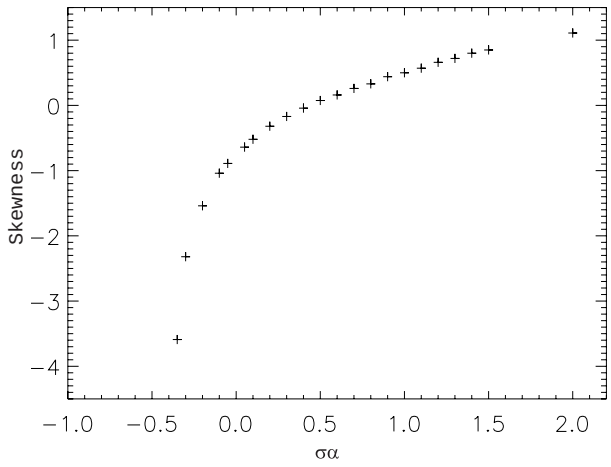

Figure 11. Variation of the skewness with the parameter $\sigma\alpha$, as predicted by the phenomenological model.

where the coefficient ν is related to the size of the computational domain. The parameter α is a combination of the bi-Maxwellian distance to threshold and of the value of $\beta_\perp$ given by

$$\alpha = \frac{2\epsilon\chi\beta_\perp}{1+\beta_\perp} = \frac{2\beta_\perp}{1+\beta_\perp}\Gamma^*. \quad (36)$$

Note that in addition to the sign of σ that characterizes the system relatively to the linear instability, and to ν that fixes the domain size, the present model only involves the parameter α, related to the distance to threshold. It turns out that the magnetic field minima $B_{\min}$ are found to be independent of the value of α.

Equation (35) was integrated in a periodic domain of size $2\pi/\sqrt{\nu}$ with a pseudo spectral method based on Fourier expansions. Linear contributions, including, in addition to the term proportional to σ, the Laplacian and biLaplacian terms without the denominators, are integrated exactly. The remaining nonlinear terms

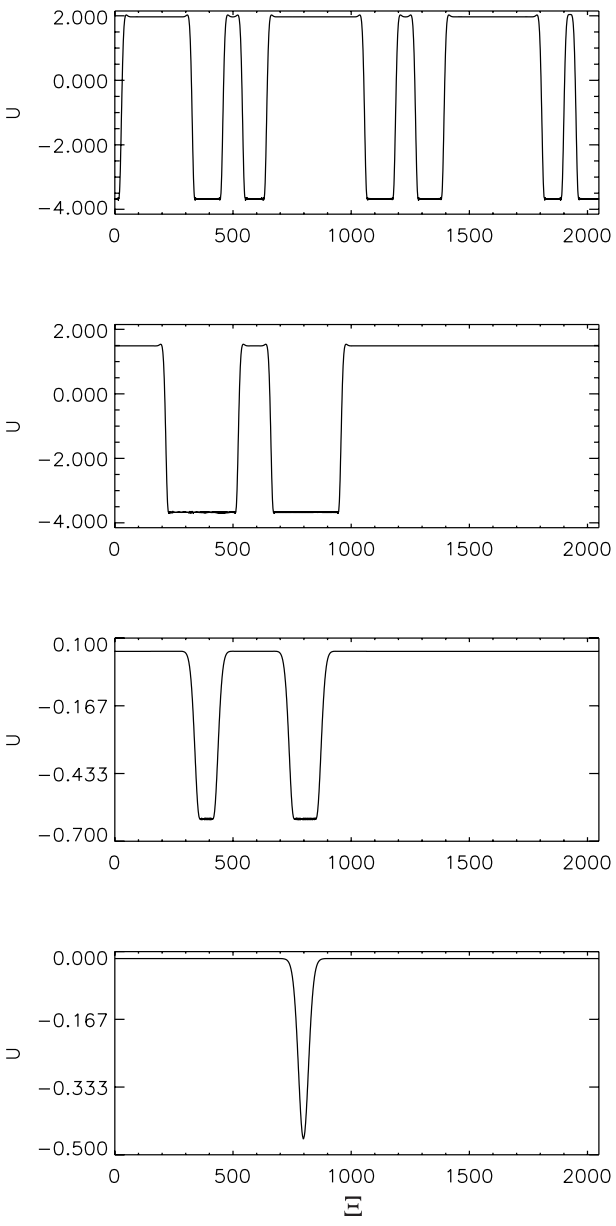

Figure 12. Magnetic holes predicted by the phenomenological model for $\sigma\alpha = 0.05, -0.05, -0.3, -0.4$ (from top to bottom), when initialized with a random noise of small amplitude when $\sigma = +1$ (over threshold) and of large amplitude when $\sigma = -1$ (below threshold).

are treated with a second-order Adams-Bashforth scheme. A first integration of the model equation above threshold ($\sigma = +1$) was performed in a domain containing 512 grid points, with $\nu = 0.01$ and starting with a small random noise. Furthermore, $\beta_\parallel = 6$ and $T_\perp/T_\parallel = 1.25$, which corresponds to $\alpha = 1.54$. We observe the formation of magnetic humps whose number decreases as time elapses, by a coarsening process very similar to that observed in the Vlasov simulations when assuming the same plasma parameters. Figure 10 exemplifies this evolution by displaying four snapshots at times $t = 3$, 5, 9 and 10. As already mentioned, the formation of magnetic humps when the variations of the local Larmor radius is retained can be understood on the basis that in regions of weak magnetic field (and large perpendicular temperatures), the ion Larmor radius is larger, making the stabilizing effect of finite Larmor radius corrections more efficient than in the linear regime. The mirror instability is thus more easily quenched in magnetic field minima than in maxima, making magnetic humps more likely to form.

In order to address the influence of the parameter α on the nature of the magnetic structures, we proceed as *Génot et al.* [2006], and introduce the third standardized moment or skewness S of the magnetic fluctuations, defined as the ratio of the third moment about the mean divided by the third power of the standard deviation. It is noticeable that S is not constant during the simulation, in that it displays significant jumps each time a structure disappears. Nevertheless, after a few steps, the coarsening becomes extremely slow and we resorted to retain the value of the skewness in this quasi-stationary regime. The resulting variation of the skewness with the parameter α is displayed in Figure 11 that summarizes the results of a series of simulations, starting with an initial random perturbation whose amplitude is small in the simulations above threshold and much larger below threshold. These simulations were performed in a domain containing 2048 grid points with $\nu = 10^{-3}$. The formation of magnetic holes is illustrated in Fig 12 which displays various structures which develop with a negative skewness. Slightly above threshold ($\alpha = 0.05$), deep holes are formed whose minima are narrow and flat. In the subcritical case and the same value of α, holes are wider and magnetic field maxima slightly smaller, but the minima are identical. As the value of $\sigma\alpha$ is decreased to -0.3 and -0.4, holes become less deep in this unit (their depth remains the same in physical units) and more spiky. Below this value of $\sigma\alpha$, the structure relaxes after a while towards the trivial solution.

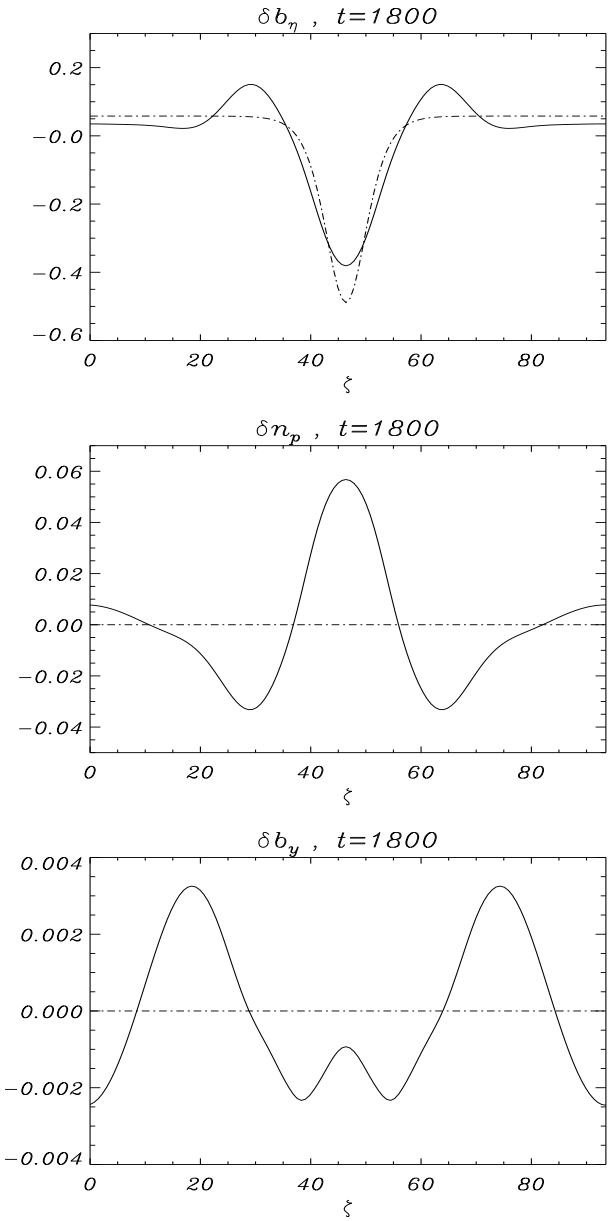

Figure 13. Persistence of initial perturbations in the form of a magnetic hole (top) and resulting density hump (middle) for $\beta_\parallel = 6$ and $T_\perp/T_\parallel = 1.36$, with $\theta = 83.82°$. The bottom panel displays the magnetic field component in the direction perpendicular to the plane defined by the ambient field and the direction of spatial variation.

6. Persistence of Large-Amplitude Magnetic Holes

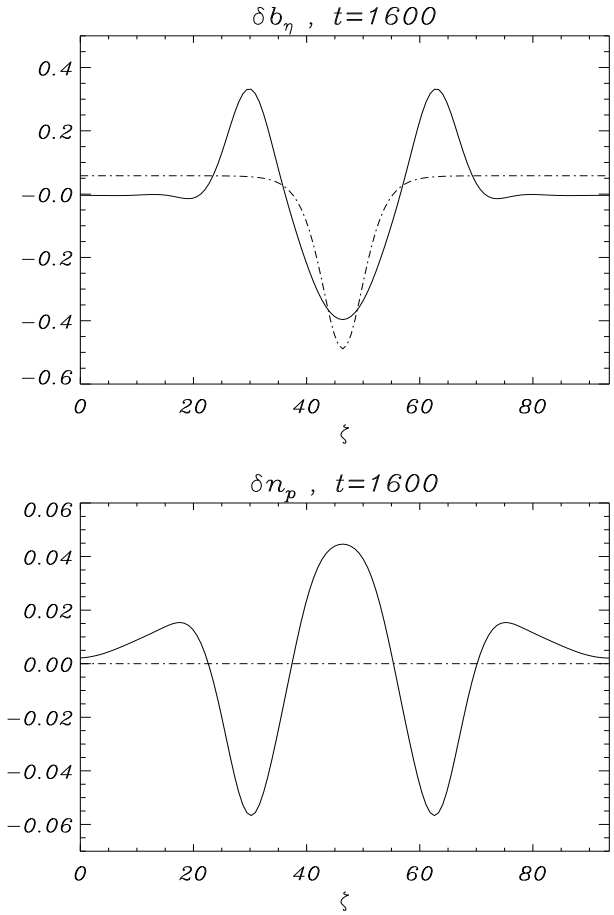

Figure 14. Persistence of a magnetic hole (top) and resulting density hump (bottom) at relatively large distance from threshold ($\beta_\parallel = 15$, $T_\perp/T_\parallel = 1.5$, with $\theta = 83.82°$).

In the previous sections, we presented numerical evidence that the nonlinear development of the mirror instability leads to the formation of magnetic humps (and density holes). Magnetic holes are also predicted below threshold by the model discussed in Section 5.2, as an effect of bistability. It is thus of interest to ask whether initially prescribed large-amplitude magnetic depressions are preserved by the evolution of the VM equations in a mirror unstable plasma. For this purpose, we performed Eulerian integrations of these equations in the conditions described above, using $\beta_\parallel = 6$, $\theta = 83.82^\circ$ and $T_\perp/T_\parallel = 1.36$, a regime close to the instability threshold. The run is initialized with a strong magnetic hole with a maximal amplitude exceeding 50% of the ambient field magnitude, with no density perturbations. We observe on Figure 13 the formation of a density hump and the persistence of the magnetic hole that evolves slightly, leading to the development of an overshoot qualitatively similar to Cluster observations reported in *Génot et al.* [2006]. A similar evolution is observed in Figure 14 at larger distance from threshold ($\beta_\parallel = 6$, $T_\perp/T_\parallel = 1.5$). The overshoot is however more important.

In order to test the bistability regime, we used the same initial conditions and kept all the plasma parameters fixed, except that now the plasma is strongly stable ($\beta_\parallel = 6$, $T_\perp/T_\parallel = 1$). Figure 15 shows than in this case also magnetic holes are preserved but, in contrast with the supercritical regime, do not develop overshoots. Note that in such a stable plasma, initial magnetic humps with no density perturbations cannot maintain, the system rapidly relaxing to the trivial solution. A detailed theory of the geometry of the nonlinear mirror structures is delicate. A partial understanding is nevertheless provided by an energy minimization argument in the simplified framework of usual anisotropic magnetohydrodynamics [*Passot et al.*, 2006]. The component of the magnetic field perpendicular to the $(\mathbf{k}, \mathbf{B}_0)$ plane, is like the longitudinal component, symmetric with respect to the center of the magnetic hole (Figure 13, bottom). This property contrasts with all previous soliton models based on anisotropic Hall-MHD [*Stasiewicz*, 2004a, b; *Mjølhus*, 2006], where it is found to be antisymmetric. Similar signatures are observed in hybrid PIC simulations of non-propagating rarefractive solitary structures generated by particle injection [*Baumgärtel et al.*, 2005]. Their symmetry properties however suggest that they do not correspond to the same branch of solutions as the slow magnetosonic solitons, in contrast with the claim by *Stasiewicz* [2004b].

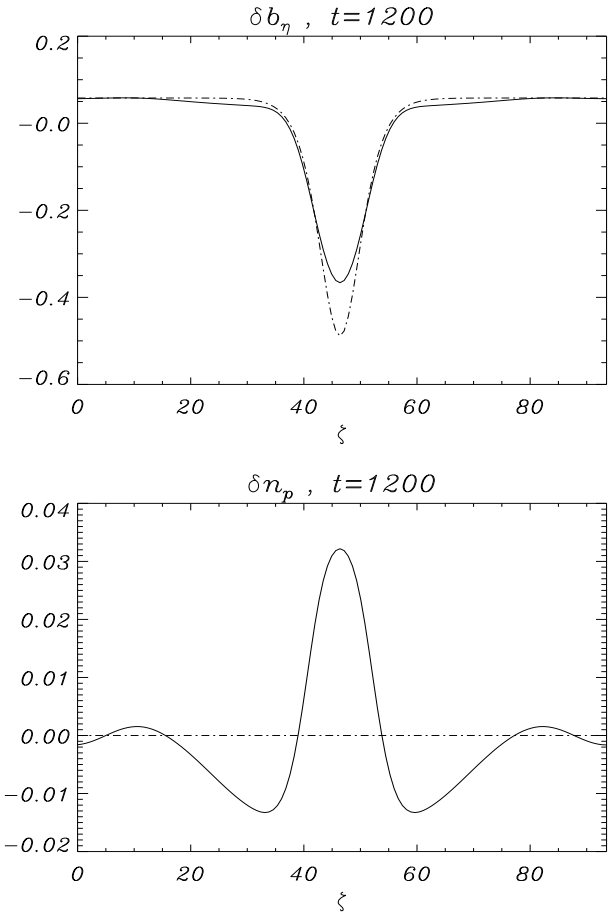

Figure 15. Persistence of a magnetic hole (top) and resulting density hump (bottom), in a plasma with $T_\perp = T_\parallel$ and $\beta_\parallel = 6$, with $\theta = 83.82^\circ$.

7. Mirror Instability Far from Threshold

In order to address the nonlinear development of the mirror instability far from threshold, we performed hybrid PIC simulations in an extended domain with $\beta_\parallel = 1$ and $T_\perp/T_\parallel = 4$, with $\theta = 50.5^\circ$ corresponding to a maximum growth rate $\gamma = 0.156\,\Omega_p$.

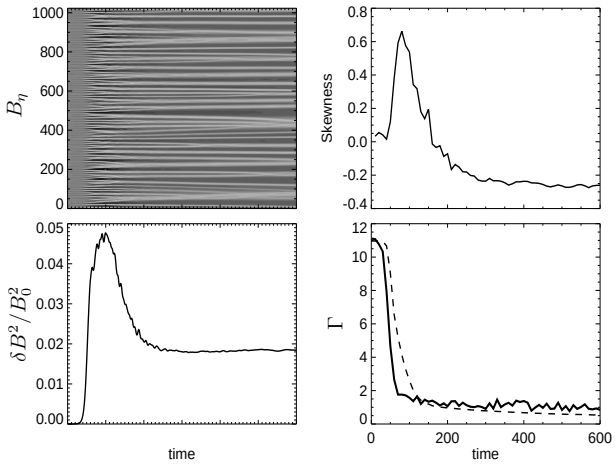

Figure 16. Evolution in an extended domain, for $\beta_\parallel = 1$, $T_\perp/T_\parallel = 4$ and $\theta = 50.5^\circ$. Gray scale plot of the magnetic fluctuation B_η as a function of time and space (left top); Time evolution of skewness of B_η (right top), of fluctuating magnetic energy $\delta B^2/B_0^2$ (left bottom), of the instantaneous distance from the threshold (right bottom): Γ (solid line) as given by equation (1) and the corresponding bi-Maxwellian value Γ^* (dashed line) obtained from equation (2).

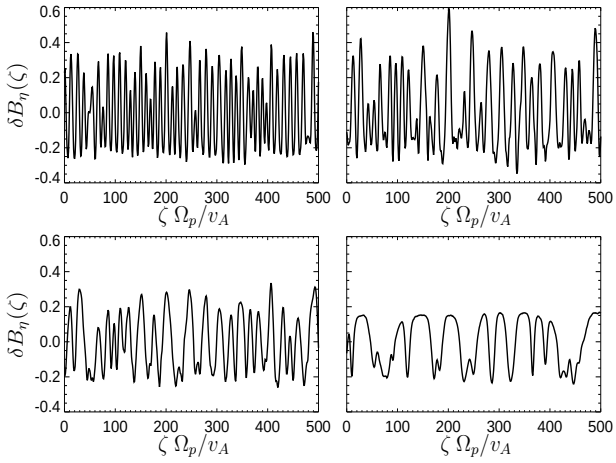

Figure 17. Profiles of δB_η as a function of ζ in a fraction of the simulation box, in the conditions of Figure 16. From left to right and top to bottom: $t = 60/\Omega_p$, $t = 100/\Omega_p$, $t = 150/\Omega_p$ and $t = 600/\Omega_p$.

Figure 16 displays the evolution in the same format as in Figure 1. A large number of magnetic humps is formed in the early nonlinear phase. They evolve in time but coarsening turns out to be significantly less efficient than close to threshold. Furthermore, at long times (typically $t > 100\,\Omega_p^{-1}$), one can observe a slow motion of some of the structures. Other important differences with respect to the simulation near threshold (Section 4.1) are visible on the skewness (Figure 16, right top) and on the energy of magnetic fluctuations (Figure 16, left bottom) that, after a brief increase, both display a significant decay. In particular the skewness becomes negative, which reflects a transformation of the early-time magnetic humps into magnetic depressions. This transition is illustrated in Figure 17 that displays the magnetic fluctuations in a quarter of the computational domain, at various instants of time: while magnetic humps are visible at early times, the long-time regime (Figure 17, right bottom) clearly displays magnetic holes.

Another important difference concerns the parameter Γ that measures the distance from threshold, as well as the bi-Maxwellian estimate Γ^*. They vary in a similar way, remaining close to each other (Figure 16, right bottom). In contrast with the near-threshold simulation in a similar computational domain, Γ saturates at a positive value that is essentially preserved until the end of the simulation. The proximity of Γ and Γ^* indicates that the distribution remains essentially bi-Maxwellian. This property is supported by inspection of the distribution functions displayed in Figure 18. The changes $\Delta\langle f\rangle$ affect a broader region of the velocity space than in the near-threshold simulation and it is compatible with a difference between two, essentially bi-Maxwellian distribution functions. Detailed analysis of the profile $\langle f\rangle$ confirms this Gaussian form (except in the wings).

A significant result of this simulation concerns the transition from magnetic humps to holes. The question arises of the role of the parameter $\beta_\parallel$ which, together with the distance from threshold, control the instability dynamics. We noted the importance of $\beta_\parallel$ by performing a similar simulation with $\beta_\parallel$ increased from 1 to 2. In the latter case, the skewness remains positive and magnetic holes do not form. This remark is consistent with the energetic stability argument given in *Passot et al.* [2006], but a detailed analysis of this transition requires further investigations.

8. Conclusion

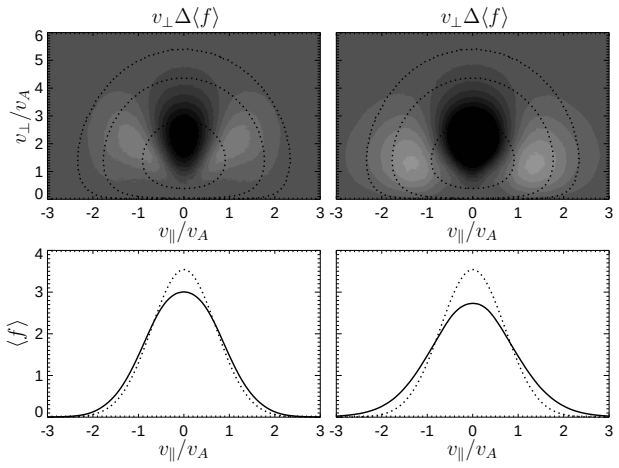

Figure 18. Same conditions as Figure 16. Simulation results at times $t = 60/\Omega_p$ (left panels) and $t = 100/\Omega_p$ (right panels): (top panels) Gray scale plots of the proton distribution variation $v_\perp\Delta\langle f\rangle$ (black corresponds to negative values and white to positive ones). Dotted lines correspond to the contours of the initial condition $v_\perp f^0$. (bottom panels) Profiles (solid line) of the proton distribution function $\langle f\rangle$ integrated over $v_\perp$, together with the initial profile (dotted line).

Numerical investigations of the mirror instability in one space dimension, based on the Vlasov-Maxwell equations, demonstrate that the nonlinear saturation is associated with the formation of magnetic humps (and anticorelated density holes). The early nonlinear dynamics near threshold is sensitive to the size of the integration domain. In an extended domain, it is indeed well described by the quasi-linear theory that involves the diffusion of particles essentially in the longitudinal velocity space and leads to a flattening of the distribution function near its maximum. After a while, the system nevertheless evolves towards a different regime, associated with the formation of coherent structures in the form of magnetic humps. During this phase, the linear growth rate calculated from the instantaneous distribution function is negative but the instability still proceeds due to hydrodynamic type nonlinearities. As time evolves, a coarsening phenomenon is observed, with only a few high amplitude peaks surviving, whose evolution becomes extremely slow. In a small domain, in contrast, the system is too much constrained to develop a quasi-linear dynamics and directly evolves towards structure formation with damped temporal oscillations viewed as the signature of particle trapping.

In order to describe the structure formation, a reductive perturbation analysis on the Vlasov-Maxwell system near threshold has been performed. It led to an asymptotic pseudo-differential equation where kinetic effects arise at a linear level only. This equation develops a finite-time singularity, indicating the existence of a subcritical bifurcation and the formation of large-amplitude structures. Saturation of the mirror instability is thus not amenable to a perturbative approach. A mechanism based on the local variations of the ion Larmor radius, was thus phenomenologically supplemented. In contrast with other models where saturation is due to the cooling of a population of trapped particles, the resulting equation correctly reproduces the dynamical evolution observed in numerical simulations of VM equations in a small computational box, such as the development of magnetic humps from an initial noise, and the existence of stable large-amplitude magnetic holes below threshold. Such simulations also display the existence of large amplitude solutions in the form of magnetic holes slightly above threshold, although there is no indication that these solutions can be obtained from direct saturation of the mirror instability.

In small domains, increasing distance from threshold does not lead to any qualitative change, but only to different values of the skewness parameter. This contrasts with the dynamics in large simulation boxes. In this case, at sufficiently large distance from threshold and for relatively small values of beta (kept nevertheless of order unity), the energy of the magnetic fluctuations displays a maximum at the time where the linear instability saturates, followed by a drastic reduction associated with the gradual transformation of magnetic peaks into magnetic holes. The instantaneous growth rate, that does not significantly depart from the bi-Maxwellian estimate, remains positive. This scenario could provide a realistic mechanism for the generation of magnetic holes in space plasmas at relatively small beta where they are indeed preferably observed [*Joy et al.*, 2006; *Soucek et al.*, 2008]. A similar transition from humps to holes is also observed in a domain that expands in time in order to model the magnetosheath plasma [*Trávníček et al.*, 2007; *Génot et al.*, 2008]. Further work is needed to address the possible relations between the results of the two simulations. Nevertheless, in both cases, the magnetic holes are not directly produced by the nonlinear saturation of the mirror instability, but are rather outcome of nontrivial nonlinear evolution. This remark could also apply to magnetic holes observed in space plasmas. To support this conjecture, we note that the simulation discussed in Section 4.1, and a similar one (with $\beta_\parallel = 3$, $T_\perp/T_\parallel = 1.4$, $\theta = 72.4^\circ$), that both involve parameters for which *Soucek et al.* [2008] observe magnetic holes, exhibit stable magnetic humps.

Several other problems remain open. From a theoretical perspective, it is interesting to ask whether there exist conditions (in very large domains and/or very close to threshold) where the mirror instability saturates by quasi-linear effects. Numerical limitations preclude to study such questions and also make difficult to obtain

evidence of the singularity predicted by the reductive perturbative expansion. These questions are probably not of importance for the understanding of mirror structures observed in space plasmas but could shed light on the role of the various microscopic phenomena that govern their formation and stability. Another interesting issue concerns the dimensionality of the structures. Again because of numerical limitations, the computations were performed in one space dimension. Such an assumption could be too constraining, especially when the beta of the plasma reaches very large values. This problem is essentially open. We nevertheless mention the work of *Constantinescu* [2002] which provides the explicit form of the linear mirror mode with axial symmetry. Furthermore, we have analyzed in the present paper simulations close to threshold where trapped particles seemed to play a rather limited role on the long-time dynamics of the mirror structures. It is natural to ask whether this conclusion still holds further away from onset, or in deep magnetic holes. Although possible mechanisms for the formation of magnetic holes have been proposed, a clear picture is still missing and observational evidences are needed to confirm or infirm the suggested ideas. In particular, a distinction between mirror structures (immobile in the plasma frame) and magnetosonic solitons (whose propagation velocity is non zero but can be quite small) could result from an analysis of their magnetic hodographs, obtained from satellite data. Another issue concerns magnetic holes observed in the solar wind by *Stevens and Kasper* [2007], whose size can reach several hundreds to one thousand ion gyroradii. Are they also associated with the mirror instability, as seemed to be implied by their analysis, and if so, by which mechanism can they reach such large sizes?

Acknowledgments. This work was performed in the framework of ISSI team "The effect of ULF turbulence and flow chaotization on plasma energy and mass transfers at the magnetopause" and the Barrande-Egide project 14226SH. The work of TP and PLS was supported by Programme Terre Soleil of CNRS. The work of EK was supported by RFBR (grant no. 06-01-00665) and by the French Ministère de l'Enseignement Supérieur et de la Recherche during his visit at the Observatoire de la Côte d'Azur which is thanked for its hospitality. The visit of TP in Pisa was supported in part by the Italian PRIN-INAF 2005. PH and PT acknowledge the support of grants GAAV No. IAA300420702 and IAA300420602, and PECS contract No. 98024. Eulerian Vlasov simulations were performed on the "Mesocentre SIGAMM" machine, hosted by Observatoire de la Côte d'Azur. Hybrid simulations have been performed on Amalka supercomputing facility at IAP, ASCR.

Appendix A: Perturbative Solution of the Vlasov Equation

We consider the Vlasov equation for the distribution function of each species (dropping the corresponding subscript index r) in the form

$$\partial_t f + (\mathbf{v}\cdot\boldsymbol{\nabla})f + \frac{q}{m}(\mathbf{E}+\mathbf{v}\times\mathbf{B})\cdot\boldsymbol{\nabla}_v f = 0, \qquad \text{(A.1)}$$

where it is convenient to express the velocity $\mathbf{v}$ in a cylindrical coordinate system by writing $\mathbf{v} = (v_\perp\cos\phi\,,\, v_\perp\sin\phi\,,\, v_\parallel)$ and $\boldsymbol{\nabla}_v = (\cos\phi\,\partial_{v_\perp} - (\sin\phi/v_\perp)\partial_\phi\,,\, \sin\phi\,\partial_{v_\perp} + (\cos\phi/v_\perp)\,\partial_\phi\,,\, \partial_{v_\parallel})$. One then has

$$(\mathbf{v}\times\mathbf{B})\cdot\boldsymbol{\nabla}_v = -B_z\partial_\phi + (\cos\phi B_y - \sin\phi B_x)\mathcal{D} + (v_\parallel/v_\perp)(\cos\phi B_x + \sin\phi B_y)\partial_\phi, \qquad \text{(A2)}$$

where $\mathcal{D} = v_\perp\partial_{v_\parallel} - v_\parallel\partial_{v_\perp}$. Furthermore, neglecting the displacement current that is irrelevant in this low-frequency asymptotics, the Maxwell equations are written

$$\frac{1}{c}\partial_t\mathbf{B} = -\nabla\times\mathbf{E} \qquad \text{(A3)}$$

$$\nabla\times\mathbf{B} = \frac{4\pi}{c}\sum_r q_r n_r\int\mathbf{v}f_r d^3v \qquad \text{(A4)}$$

$$\nabla\cdot\mathbf{E} = 4\pi\sum_r q_r n_r\int f_r d^3v. \qquad \text{(A5)}$$

As suggested by the linear instability growth rate near threshold (equation (3)), the independent variables are rescaled in the form $X = \sqrt{\varepsilon}x$, $Y = \sqrt{\varepsilon}y$, $Z = \varepsilon z$, $T = \varepsilon^2 t$, where ε measures the distance to threshold. Furthermore, suppressing the species index to simplify the writing, the proton distribution function is expanded in the form

$$f = f^{(0)} + \varepsilon f^{(1)} + \varepsilon^{3/2}f^{(3/2)} + \varepsilon^2 f^{(2)} + \cdots. \qquad \text{(A6)}$$

Similarly the magnetic field is written (we here denote by the subscript $\perp$, the transverse component of a vector whose two components are referred to by the x and y indices)

$$\mathbf{B}_\perp = \varepsilon^{3/2}\mathbf{B}_\perp^{(3/2)} + \varepsilon^{5/2}\mathbf{B}_\perp^{(5/2)} + \cdots \qquad \text{(A7)}$$

$$B_z = B_0 + \varepsilon B_z^{(1)} + \varepsilon^2 B_z^{(2)} + \cdots. \qquad \text{(A8)}$$

From the Faraday equation and the assumption of cold and massless electrons that implies $\mathbf{E}\cdot\mathbf{B} = 0$, one has for the electric field

$$\mathbf{E}_\perp = \varepsilon^{5/2}\mathbf{E}_\perp^{(5/2)} + \varepsilon^{7/2}\mathbf{E}_\perp^{(7/2)} + \cdots \qquad \text{(A9)}$$

$$E_z = \varepsilon^4 E_z^{(4)} + \varepsilon^5 E_z^{(5)}\cdots. \qquad \text{(A10)}$$

Introducing the ion gyrofrequency $\Omega = eB_0/(mc)$ and expanding the Vlasov equation to the successive orders, one first gets $\Omega\partial_\phi f^{(0)} = 0$ and $\Omega\partial_\phi f^{(1)} = 0$. The normalized equilibrium distribution function is taken bi-Maxwellian, in the form

$$f^{(0)} \equiv \frac{1}{\pi^{3/2}v_{th\parallel}v_{th\perp}^2}\exp -\Big(\frac{v_\parallel^2}{v_{th\parallel}^2} + \frac{v_\perp^2}{v_{th\perp}^2}\Big). \qquad \text{(A11)}$$

On the other hand, $f^{(1)} = \overline{f}^{(1)}$, where the overline indicates averaging on the gyroangle ϕ (the fluctuating part will be denoted by a tilde).

At the next orders, one has

$$\Omega\partial_\phi f^{(2)} = v_\perp(\cos\phi\,\partial_X + \sin\phi\,\partial_Y)f^{(3/2)} + v_\parallel\partial_Z\overline{f}^{(1)} \qquad \text{(A12)}$$

$$\Omega\partial_\phi f^{(3)} = v_\perp(\cos\phi\,\partial_X + \sin\phi\,\partial_Y)f^{(5/2)} + \partial_T\overline{f}^{(1)} + v_\parallel\partial_Z f^{(2)} + \Omega\Big[-\frac{B_z^{(1)}}{B_0}\partial_\phi f^{(2)} + \Big(\cos\phi\frac{B_y^{(3/2)}}{B_0} - \sin\phi\frac{B_x^{(3/2)}}{B_0}\Big)\mathcal{D}f^{(3/2)} + \frac{v_\parallel}{v_\perp}\Big(\cos\phi\frac{B_y^{(3/2)}}{B_0} + \sin\phi\frac{B_x^{(3/2)}}{B_0}\Big)\partial_\phi f^{(3/2)}\Big]. \qquad \text{(A13)}$$

and

$$\Omega\partial_\phi f^{(3/2)} = v_\perp(\cos\phi\,\partial_X + \sin\phi\,\partial_Y)\overline{f}^{(1)} + \Omega\Big(\cos\phi\frac{B_y^{(3/2)}}{B_0} - \sin\phi\frac{B_x^{(3/2)}}{B_0}\Big)\mathcal{D}f^{(0)} \qquad \text{(A14)}$$

$$\Omega\partial_\phi f^{(5/2)} = v_\perp(\cos\phi\,\partial_X + \sin\phi\,\partial_Y)f^{(2)} + v_\parallel\partial_Z f^{(3/2)} + \frac{q}{m}(\cos\phi\,E_x^{(5/2)} + \sin\phi\,E_y^{(5/2)})\partial_{v_\perp}f^{(0)} + \Omega\Big[-\frac{B_z^{(1)}}{B_0}\partial_\phi f^{(3/2)} + \Big(\cos\phi\frac{B_y^{(5/2)}}{B_0} - \sin\phi\frac{B_x^{(5/2)}}{B_0}\Big)\mathcal{D}f^{(0)} + \Big(\cos\phi\frac{B_y^{(3/2)}}{B_0} - \sin\phi\frac{B_x^{(3/2)}}{B_0}\Big)\mathcal{D}\overline{f}^{(1)}\Big] \qquad \text{(A15)}$$

where, for convenience, integer and non integer orders are considered separately. The solvability of equation (A15) supplemented by equations (A12) and (A14), implies $\overline{f}^{(3/2)} = 0$. Near threshold, it is useful to add the solvability conditions at the two leading orders and write from equations (A12) and (A13)

$$-v_\perp\langle(\sin\phi\,\partial_X - \cos\phi\,\partial_Y)\partial_\phi(f^{(3/2)} + \varepsilon f^{(5/2)})\rangle + (\varepsilon\partial_T + v_\parallel\partial_z)\overline{f}^{(1)} + \varepsilon v_\parallel\partial_z\overline{f}^{(2)} - \varepsilon\Omega\Big\langle\Big(\cos\phi\frac{B_x^{(3/2)}}{B_0} + \sin\phi\frac{B_y^{(3/2)}}{B_0}\Big)\Big(\mathcal{D} - \frac{v_\parallel}{v_\perp}\Big)(v_\perp\overline{f}^{(1)})\Big\rangle = 0. \qquad \text{(A16)}$$

Furthermore, equations (A14) and (A12) are solved as

$$\widetilde{f}^{(3/2)} = \frac{v_\perp}{\Omega}\Big(\sin\phi\,\partial_X - \cos\phi\,\partial_Y\Big)\overline{f}^{(1)} + \Big(\sin\phi\frac{B_y^{(3/2)}}{B_0} + \cos\phi\frac{B_x^{(3/2)}}{B_0}\Big)\mathcal{D}f^{(0)} \qquad \text{(A17)}$$

and

$$\widetilde{f}^{(2)} = -\frac{v_\perp^2}{4\Omega^2}[\cos 2\phi\,(\partial_{XX}-\partial_{YY})+2\sin 2\phi\,\partial_{XY}]\overline{f}^{(1)} - \frac{1}{4\Omega}\Big[\cos 2\phi\left(\partial_X\frac{B_y^{(3/2)}}{B_0}-\partial_Y\frac{B_x^{(3/2)}}{B_0}\right) - \sin 2\phi\left(\partial_X\frac{B_x^{(3/2)}}{B_0}-\partial_Y\frac{B_y^{(3/2)}}{B_0}\right)\Big]v_\perp\mathcal{D}f^{(0)}. \tag{A18}$$

At the order of the present approximation, it is possible in (A18) to make the replacement

$$\overline{f}^{(1)} = \frac{v_\perp}{2v_\parallel}\mathcal{D}f^{(0)}\frac{B_z^{(1)}}{B_0} = -\Big(\frac{1}{v_{th\parallel}^2}-\frac{1}{v_{th\perp}^2}\Big)v_\perp^2 f^{(0)}\frac{B_z^{(1)}}{B_0} \tag{A19}$$

Defining $b_z = B_z^{(1)} + \varepsilon B_z^{(2)}$ and $\overline{F} = \overline{f}^{(1)} + \varepsilon\overline{f}^{(2)}$, it is possible at the order of the present approximation, to replace $B_z^{(1)}$ by b_z and $\overline{f}^{(1)}$ by $\overline{F}$ in the terms preceded by ε. We get

$$(\varepsilon\partial_T + v_\parallel\partial_Z)\overline{F} = -\frac{v_\perp}{2}\partial_{v_\perp}f^{(0)}(\varepsilon\partial_T+v_\parallel\partial_Z)\frac{b_z}{B_0} + \frac{v_\perp}{2}\partial_{v_\parallel}f^{(0)}\partial_Z\frac{b_z}{B_0} - \varepsilon\partial_Z A \tag{A20}$$

with

$$A = -\frac{3v_\perp^3}{16\Omega^2}\Delta_\perp\Big(\frac{b_z}{B_0}\Big)\mathcal{D}f^{(0)} - \frac{v_\perp v_\parallel}{2\Omega}\frac{4\pi}{c}j_z^{(2)}\mathcal{D}f^{(0)} + \frac{v_\perp}{4}\Big(\frac{b_z}{B_0}\Big)^2\mathcal{D}\Big(f^{(0)}-\frac{v_\perp}{2v_\parallel}\mathcal{D}f^{(0)}\Big). \tag{A21}$$

At the same order of approximation, we solve equation (A20) as

$$\overline{F} = -\frac{v_\perp}{2}\partial_{v_\perp}f^{(0)}\frac{b_z}{B_0} + (\varepsilon\partial_T+v_\parallel\partial_Z)^{-1}\frac{v_\perp^2}{2}\partial_{v_\parallel}f^{(0)}\partial_Z\frac{b_z}{B_0} - \varepsilon\frac{A}{v_\parallel}, \tag{A22}$$

where, as shown in Appendix B, $j_z^{(2)}=0$ and, consequently, A is in fact proportional to $v_\parallel$.

Appendix B: Consequences of Ampère Equation

To leading order, equation (A4) gives

$$\partial_Y B_z^{(1)} = \frac{4\pi}{c}\sum_r q_r n_r\int v_\perp\cos\phi\,\widetilde{f}_r^{(3/2)}d^3v = -\frac{4\pi}{c}\sum_r q_r n_r\frac{1}{\Omega_r}\int\frac{v_\perp^2}{2}\partial_Y\overline{f}_r^{(1)}d^3v. \tag{B1}$$

Using equations (A19), one easily checks that for cold electrons, only the ions contribute to the current, leading to the threshold condition for the mirror instability, in the form

$$0 = \beta_\perp\Big(\frac{T_\perp^{(0)}}{T_\parallel^{(0)}}-1\Big)-1 \tag{B2}$$

or (see equation (2)),

$$\Gamma^* = 0. \tag{B3}$$

Here $\beta_\perp = v_{th\perp}^2/v_A^2$ where $v_{th\perp}$ is the ion perpendicular thermal velocity and $v_A = B_0/(4\pi mn)^{1/2}$ the Alfvén speed.

On the other hand,

$$\partial_X B_y^{(3/2)} - \partial_Y B_x^{(3/2)} = \frac{4\pi}{c}j_z^{(2)} = \varepsilon^{-1}\frac{4\pi}{c}\sum_r q_r n_r\int v_\parallel\overline{F}_r d^3v. \tag{B4}$$

Since $\overline{F}$ is an even function of $v_\parallel$, equation (A22) then implies

$$j_z^{(2)} = \varepsilon^{-1}\int v_\parallel(\varepsilon\partial_T+v_\parallel\partial_Z)^{-1}\frac{v_\perp}{2}\partial_{v_\parallel}f^{(0)}d^3v\,\partial_Z\frac{b_z}{B_0} - \int\frac{v_\perp v_\parallel}{2\Omega}\frac{4\pi}{c}j_z^{(2)}\mathcal{D}f^{(0)}d^3v \tag{B5}$$

The first term in the RHS does not contribute. The resulting equality then prescribes $j_z^{(2)}=0$.

Appendix C: Estimate of the Pressure Tensor

When dealing with the perpendicular pressure fluctuations, we define

$$\overline{p}_\perp = p_\perp^{(1)} + \varepsilon p_\perp^{(2)} = (mn/2)\int v_\perp^2\overline{F}d^3v. \tag{C.1}$$

Using equations (A22) and (A21), we obtain

$$\overline{p}_\perp = \beta_\perp\Big(1-\frac{\beta_\perp}{\beta_\parallel}\Big)\frac{B_0 b_z}{4\pi} + \varepsilon\frac{\sqrt{\pi}}{v_{th\,\parallel}}\partial_T\Big(-\mathcal{H}\,\partial_Z\Big)^{-1}\frac{\beta_\perp^2}{\beta_\parallel}\frac{B_0 b_z}{4\pi} - \varepsilon p_\perp^{(0)}\Big[\frac{9}{4\beta_\perp}r_L^2\Delta_\perp\frac{b_z}{B_0} + \Big(1-4\frac{\beta_\perp}{\beta_\parallel}+3\frac{\beta_\perp^2}{\beta_\parallel^2}\Big)\Big(\frac{b_z}{B_0}\Big)^2\Big]. \tag{C2}$$

Here $\mathcal{H}$ is the Hilbert transform along the direction of the ambient magnetic field. The operator $-\mathcal{H}\,\partial_Z$ is thus a positive operator whose Fourier transform reduces to $|K_z|$, where K_z denotes the variable conjugated to Z.

The leading order contributions of the nongyrotropic components of the pressure tensor are given by

$$\Pi_{xx}^{(2)} = -\frac{mn}{2}\int v_\perp^2\cos 2\phi\,\widetilde{f}^{(2)}d^3v \tag{C3}$$

$$\Pi_{xy}^{(2)} = \frac{mn}{2}\int v_\perp^2\sin 2\phi\,\widetilde{f}^{(2)}d^3v \tag{C4}$$

$$\Pi_{xz}^{(3/2)} = mn\int v_\parallel v_\perp\cos\phi\,\widetilde{f}^{(3/2)}d^3v + (p_\perp^{(0)}-p_\parallel^{(0)})\frac{B_x^{(3/2)}}{B_0}, \tag{C5}$$

that are easily computed as

$$\Pi_{xx}^{(2)} = -\frac{mn}{16\Omega^2}\int v_\perp^4(\partial_{XX}-\partial_{YY})\overline{f}^{(1)}d^3v = -\frac{3}{4}\Big(1-\frac{\beta_\perp}{\beta_\parallel}\Big)p_\perp^{(0)}r_L^2(\partial_{XX}-\partial_{YY})\frac{B_z^{(1)}}{B_0} \tag{C6}$$

$$\Pi_{xy}^{(2)} = -\frac{mn}{8\Omega^2}\int v_\perp^4\partial_{XY}\overline{f}^{(1)}d^3v = -\frac{3}{2}\Big(1-\frac{\beta_\perp}{\beta_\parallel}\Big)p_\perp^{(0)}r_L^2\partial_{XY}\frac{B_z^{(1)}}{B_0} \tag{C7}$$

$$\Pi_{xz}^{(3/2)} = 0. \tag{C8}$$

As a consequence,

$$\Big(\boldsymbol{\nabla}\cdot\boldsymbol{\Pi}\Big)_\perp^{(5/2)} = -\frac{3}{4}\Big(1-\frac{\beta_\perp}{\beta_\parallel}\Big)p_\perp^{(0)}r_L^2\Delta_\perp\boldsymbol{\nabla}_\perp\frac{B_z^{(1)}}{B_0}. \tag{C9}$$

References

Baumgärtel, K. (1999), Soliton approach to magnetic holes, *J. Geophys. Res.*, *104*(A12), 28295–28308.

Baumgärtel, K., E. Dubinin, K. Sauer, and T.R. Story (1997), Solar wind magnetic holes: signature of slow mode type MHD solitons? *Adv. Space Res.*, *20*, 69–74.

Baumgärtel, K., K. Sauer, and E. Dubinin (2003), Towards understanding magnetic holes: Hybrid simulations, *Geophys. Res. Lett.*, *30*, 1761, doi: 10.1029/2003GL017373.

Baumgärtel, K., K. Sauer, and E. Dubinin (2005), Kinetic slow mode-type solitons, *Nonlin. Proc. Geophys.*, *12*, 291–298.

Constantinescu, O.D. (2002), Self-consistent model of mirror structures, *J. Atm. Solar-Terrestrial Phys.*, *64*, 645-649.

Gary, S. P. (1992), The mirror and ion cyclotron anisotropy instabilites, *J. Geophys. Res.*, *97*, 8519–8529.

Génot, V., E. Budnik, C. Jacquey, J. Sauvaud, I. Dandouras, and E. Lucek (2006), Statistical study of mirror mode events in the Earth magnetosheath, *AGU Fall Meeting Abstracts*, *C1412+*.

Génot, V., E. Budnik, P. Hellinger, T. Passot, G. Belmont, P. Trávníček, P. L. Sulem, E. Lucek, and I. Dandouras, Mirror structures above and below the linear instability threshold: Cluster observations, fluid model and hybrid simulations, *Ann. Geophys.*, submitted, 2008.

Hall, A. N. (1979), Finite ion Larmor radius modifications to the firehose and mirror instabilities, *J. Plasma Phys.*, *21*, 431–443.

Hasegawa, A. (1969), Drift mirror instability in the magnetoshere, *Phys. FLuids*, *12*, 2642–2650.

Hellinger, P. (2007), Comment on the linear mirror instability near threshold, *Phys. Plasmas*, *14*, 082105.

Hellinger, P., and P. Trávníček (2005), Magnetosheath compression: Role of characteristic compression time, alpha particle abondance and alpha/proton relative velocity, *J. Geophys. Res.*, *110*, A04210, doi: 10.1029/2004JA010687.

Horbury, T. S., E. A. Lucek, A. Bulogh, I. Dandouras, and H. Rème (2004), Motion and orientation of magnetic field dips and peaks in the terrestrial magnetosheath, *J. Geophys. Res.*, *109*, A09202, doi: 10.1029/2003JA010237.

Joy, S. P., M. G. Kivelson, R. J. Walker, K. K. Khurana, C. T. Russell, and W. R. Paterson (2006), Mirror mode structures in the Jovian magnetosheath, *J. Geophys. Res.*, *111*, A12212, doi:10.1029/2006JA011985.

Kaufmann, R. L., J. T. Horng, and A. Wolfe (1970) Large amplitude hydromagnetic waves in the inner magnetosheath, *J. Geophys. Res.*, *75*, 4666–4667.

Kivelson, M. G., and D. S. Southwood (1996), Mirror instability II: The mechanism of nonlinear saturation, *J. Geophys. Res.*, *101*, 17,365–17,372.

Kuznetsov, E. A., T. Passot, and P. L. Sulem (2007), A dynamical model for nonlinear mirror modes near threshold, *Phys. Rev. Lett.*, *98*, 235003.

Kuznetsov, E. A., T. Passot, and P. L. Sulem (2007), Nonlinear theory of mirror instability near threshold, *Pis'ma v ZhETF*, *86*, 725–730; *JETP Lett.*, *86* (10) 637–642.

Leckband J.A., D. Burgess, F.G.E. Pantellini, and S.J. Schwartz (1995) Ion distributions associated with mirror waves in the earth magnetosheath, *Adv. Space Res.*, *15*, 345–348.

Lucek, E. A., M. W. Dunlop, A. Balogh, P. Cargill, W. Baumjohann, E. Georgescu, G. Haerendel, and K. H. Fornacon (1999), Mirror mode structures observed in the dawn-side magnetosheath by Equator-S, *Geophys. Res. Lett.*, *26*, 2159–2162.

Mangeney, A., F. Califano, C. Cavazzioni, and P. Trávníček (2002), A numerical scheme for the integration of the Vlasov-Maxwell system of equations, *J. Comput. Phys.*, *179*, 495–538.

Matthews, A. (1994), Current advance method and cyclic leapfrog for 2D multi-species hybrid plasma simulations, *J. Comput. Phys.*, *112*, 102–116.

McKean, M. E., D. Winske, and S. P. Gary (1992), Mirror and ion cyclotron anisotropy instabilities in the magnetosheath, *J. Geophys. Res.*, *97*, 19,421–19,432.

McKean, M. E., D. Winske, and S. P. Gary (1994), Two-dimensional simulations of ion anisotropy instabilities in the magnetosheath, *J. Geophys. Res. 99*, 11,141–11,153.

Mjølhus, E. (2006), Velocity-amplitude relationships and polarization in families of MHD solitary waves, *Phys. Scr.*, *T122*, 135–153.

Pantellini, F. G. E. (1998) A model of the formation of stable nonpropagating magnetic structures in the solar wind based on the mirror instability, *J. Geophys. Res.*, *103*, 4789–4798.

Pantellini, F. G. E., D. Burgers, and S. J. Schwartz (1995), On the non-linear mirror instability, *Adv. Space Res.*, *15*, 341–344.

Passot, T., V. Ruban, and P. L. Sulem (2006), Fluid description of trains of stationary mirror structures in a magnetized plasma, *Phys. Plasmas*, *13*, 102310.

Pokhotelov, O. A., M. A. Balikhin, R. Z. Sagdeev, and R. A. Treumann (2005), Halo and mirror instabilities in the presence of finite Larmor radius effects, *J. Geophys. Res.*, *110*, A10206, doi: 10.1029/2004JA010933.

Pokhotelov, O. A., R. Z. Sagdeev, M. A. Balikhin,O. G. Onishchenko, and V. Fedun (2007), Nonlinear mirror waves in non-Maxwellian space plasmas: collapse or solitons? *Lecture Notes of the 2007 Summer College on Plasma Physics* 1856-36, Abdus Salam International Center for theoretical Physics, Trieste.

Price, C. P., D. W. Swift, and L.-C. Lee (1986), Numerical simulation of nonoscillatory mirror waves at the Earth's magnetosheath, *J. Geophys. Res.*, *91*, 101–112.

Shapiro, V. D., and V. I. Shevchenko (1964), Quasilinear theory of instability of a plasma with an anisotropic ion velocity distribution, *Sov. Phys. JETP*, *18*, 1109–1116.

Soucek, J., E. Lucek, and I. Dandouras (2008), Properties of magnetosheath mirror modes observed by Cluster and their responses to changes in plasma parameters, *J. Geophys. Res.*, *113*, in press, doi: 10.1029/2007JA012649.

Southwood, D. J., and M. G. Kivelson (1993) Mirror instability: 1. Physical mechanism of linear instability, *J. Geophys. Res.*, *98*, 9181–9187.

Sperveslage, K., F. M. Neubauer, K. Baumgärtel, and N. F. Ness (2000), Magnetic holes in the solar wind between 0.3 AU and 17 AU, *Nonlin. Proc. Geophys.*, *7*, 191–200.

Stasiewicz, K. (2004a) Theory and Observations of Slow-Mode Solitons in Space Plasmas, *Phys. Rev. Lett.*, *93*, 125004.

Stasiewicz, K. (2004b) Reinterpretation of mirror modes as trains of slow magnetosonic soltions, *Geophys. Res. Lett.*, *31*, L21804, doi: 10.1029/2004GL021282.

Stevens, M. L., and J. C. Kasper (2007), A scale-free analysis of magnetic holes at 1 AU, *J. Geophys. Res.*, *112*, A05109, doi: 10.1029/2006JA012116.

Trávníček, P., P. Hellinger, M. G. G. T. Taylor, C. P. Escoubet, I. Dandouras, and E. Lucek (2007), Magnetosheath plasma expansion: Hybrid simulations, *Geophys. Res. Lett.*, *34*, L15104, doi:10.1029/2007GL029728.

Valentini, F., P. Trávníček, F. Califano, P. Hellinger, and A. Mangeney (2007), A hybrid-Vlasov model based on the current advance method for the simulation of collisionless magnetized plasma, *J. Comput. Phys.*, *225*, 753–770.

Vedenov, A. A., and R. Z. Sagdeev (1959), Plasma Physics and Problem of Controlled Thermonuclear Reactions, Vol. III, ed. M. A. Leontovich, 332-339, (English edition, Pergamon, NY).

F. Califano, Dipartimento di Fisica and CNISM, Universitá di Pisa, Largo Pontercorvo n.3, 56127 Pisa, Italy (califano@df.unipi.it)

P. Hellinger and P. Trávníček, Institute of Atmospheric Physics, AS CR Bocni II/1401, 14131 Prague, Czech Republic (petr.hellinger@ufa.cas.cz, trav@Alenka.ufa.cas.cz)

E. Kuznetsov, P.N. Lebedev Physical Institute, 53 Leninsky Avenue, 119991 Moscow, Russia and L.D. Landau Institute of Theoretical Physics, 2 Kosygin Street, 119334 Moscow, Russia (kuznetso@itp.ac.ru)

T. Passot and P.L. Sulem, Université de Nice-Sophia Antipolis, CNRS, Observatoire de la Côte d'Azur, B.P. 4229, 06304 Nice Cedex 4, France (passot@oca.eu, sulem@oca.eu)